5

DIPOLES, SLOTS, AND LOOPS

A dipole is a conductive rod usually split in the center and fed from a balanced transmission line that carries equal and oppositely flowing currents. Not all dipoles are split and fed in the center because currents can be excited on it electromagnetically or it can be shunt fed. The dipole length determines possible current distributions in modes, and when we place a continuous rod near an antenna radiating a linear polarization component directed along the rod, it excites a standing-wave current on the rod. The amount excited on the rod depends on how close its length is to resonance and the antenna spacing. Of course, the continuous rod loads the fed antenna through mutual coupling. We can feed the continuous rod from a coax line by attaching the outer conductor to the center and then connecting the center conductor away from the center in a shunt feed.

A slot is a narrow-width opening in a conductive sheet. When excited by a voltage across the narrow dimension it appears to radiate from an equivalent magnetic current flowing along the long dimension that replaces the voltage (or electric field) across it. Most slots, similar to dipoles, have a finite length with either short or open circuits at both ends. The voltage along the slot forms a standing wave. Of course, magnetic currents are fictitious, and real electric currents flow in the conductive sheet around the slot. These currents do not have a simple distribution and are difficult to use for analysis, so we use simpler magnetic currents, although when analyzing a slot using the method of moments, we model the conductors around the slot and calculate patterns, reaction, and so on, from these real currents. Initial slot calculations assume that the conductive sheet is infinite, similar to the analysis of dipoles situated in free space. Complete analysis of the dipole requires analysis in the presence of the mounting configuration. Similarly, full analysis of slots includes the effects of the finite sheet and scattering from the objects around it.

After considering ideal cases, we analyze the effects of finite ground planes, nearby scatterers, and the interaction between dipoles and slots. The batwing antenna presents an unusual case where the antenna at first glance looks like a dipole but actually radiates from a combination of a slot and a finite dipole structure. Another interesting case is the waveguide slot. Currents flow on the inside surfaces of a waveguide, and the finite current skin depth prevents it from reaching the outside. The metal walls shield the currents and prevent the loss of power by radiation. When we cut a slot in the wall, the internal currents flow out the slot and onto the outside of the waveguide and radiate. The excitation and length of the slot relative to the internal currents determine the amount radiated. Similarly, the slots load the waveguide as a transmission line because of the loss of power.

Our analysis starts with a dipole in free space or a slot on an infinite conductive sheet. The two problems are duals. Dipoles radiate from a standing-wave electric (real) current, whereas the slot radiates from a standing-wave magnetic current. We use the same mathematics for both patterns. By the Babinet–Booker principle of complementary structures, we relate the input impedance of one to the other. Both structures radiate the same pattern but differ in polarization. Dipoles and slots share the same analysis through duality, so we develop them together. Singly and in arrays, they satisfy many antenna needs. Although they share a dual analysis, they have unique feeding requirements. We discuss baluns for dipoles and waveguide slot excitations as practical implementations.

In Chapter 2 we presented the analysis of a small loop excited with a uniform current (Section 2-1.2). The loop current was replaced with a small magnetic current element flowing along the normal to the plane of the loop. Multiple turns and ferrite loading increase the efficiency of loops and produce a more useful antenna. Exciting a uniform current on a loop is a difficult task that offers little practical benefit. The loops discussed will have standing-wave electric currents excited on them determined by feeding methods. The natural balun used to excite a small loop produces a standing-wave current with zero current at the point where the two sides are connected to form the loop. A resonant length loop of about one wavelength perimeter radiates a dipole pattern from a standing-wave current. The quadrifilar helix consists of two loops twisted around a common axis. The twist produces currents that radiate circular polarization from each loop. Analysis shows that the currents are standing wave.

Feeding a dipole or loop requires a balun to prevent current flow either along the outside of a coaxial feeder or excitation of unbalanced currents along a two-wire line. The current flowing along the outside of the coax or unbalanced currents on the two-wire line radiate in unwanted directions or radiate undesired polarization. When we design an antenna without considering or knowing its final mounting, we produce an uncontrolled situation without a balun. Our initial configuration may work without a balun, but the antenna may fail to produce the desired pattern in the final location. If you control the installation completely, you can reduce your design effort and may be able to eliminate the balun.

5-1   STANDING-WAVE CURRENTS

Think of a dipole as a diverging two-wire transmission line. The characteristic impedance increases as the wave approaches the open-circuited ends. The slot is the
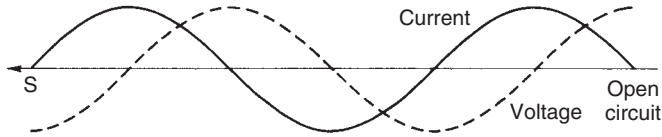
FIGURE 5-1 Standing wave.

dual of a strip dipole. A voltage excited across the slot propagates along a slotline toward short-circuited ends. Each type of transmission line reflects the incident wave from the terminations. The combination of two waves traveling in opposite directions creates a standing wave on the line. The current and voltage are 90° out of phase and 90° out of space phase (Figure 5-1). Current and voltage change places on the short-circuited termination of the slot.

The dipole is not a uniform transmission line, but we can approximate the current as a standing wave with the current vanishing on the ends. The slot voltage is a standing wave also vanishing on the ends. The standing waves for a center-fed dipole or slot are expressed as follows:

$$
\begin{array}{ll}
\text{Dipole} & \text{Slot} \\
I = I_0 \sin k\left(\dfrac{L}{2} - z\right) \qquad V = V_0 \sin k\left(\dfrac{L}{2} - z\right) & z \geq 0 \\[2mm]
I = I_0 \sin k\left(\dfrac{L}{2} + z\right) \qquad V = V_0 \sin k\left(\dfrac{L}{2} + z\right) & z \leq 0
\end{array}
\tag{5-1}
$$

The voltage distribution on the slot is equivalent to a magnetic current.

We calculate radiation from the linear sinusoidal current distributions by the vector potentials: electric (slot) (Section 2-1.2) and magnetic (dipole) (Section 2-1.1). Figure 5-2 gives typical sinusoidal distributions for various lengths. The currents match at the feed point and vanish on the ends. Consider the pattern of the 2λ dipole at $\theta = 90°$. We can assume that it is a continuous array and sum the fields from each
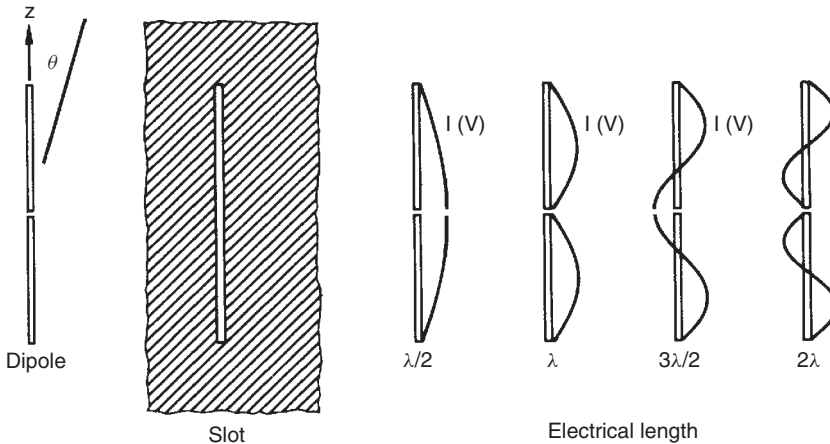
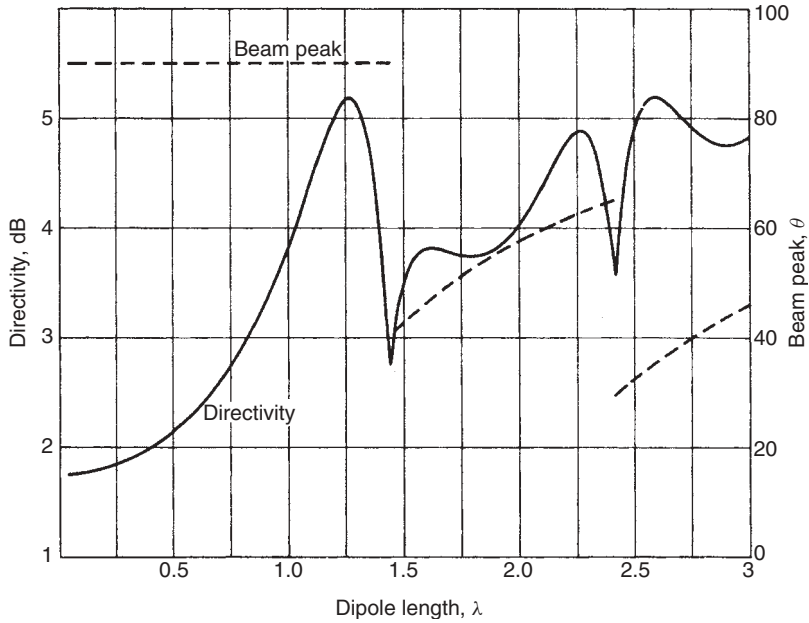**FIGURE 5-2** Sinusoidal distributions.

FIGURE 5-3   Dipole (slot) directivity and beam peak versus length.

portion along the axis. The equal positive and negative portions of the standing-wave current sum to zero and produce a pattern null normal to the axis. By integrating Eqs. (2-5) and (2-10), we compute far fields for radiators centered on the z-axis through the far-field conversion [Eqs. (2-1) and (2-9)] [1, p. 82]:

$$E_\theta = j\eta \frac{I_0}{2\pi r} e^{-jkr} \frac{\cos(kL/2 \cos\theta) - \cos(kL/2)}{\sin\theta} \qquad \text{dipole} \qquad (5\text{-}2)$$

where L is the total dipole length. Using the $Y = 0$ plane as the slot ground plane, the far-field magnetic field is found as

$$H_\theta = \frac{\pm jV_0}{\eta 2\pi r} e^{-jkr} \frac{\cos(kL/2 \cos\theta) - \cos(kL/2)}{\sin\theta} \qquad \text{slot} \qquad (5\text{-}3)$$

where L is the total slot length. We apply the upper sign for $Y > 0$ and the lower sign for $Y < 0$. The electric field of the slot is found from $E_\phi = -\eta H_\theta$. Equations (5-2) and (5-3) have the same pattern shape and directivity. We integrate the magnitude squared of Eqs. (5-2) and (5-3) to determine the average radiation intensity. Joined with the maximum radiation intensity, we calculate directivity (Figure 5-3) versus length.

5-2 RADIATION RESISTANCE (CONDUCTANCE)

The far-field power densities, Poynting vectors, are given by

$$S_r = \begin{cases} \dfrac{|E_\theta|^2}{\eta} & \text{dipole} \\ |H_\theta|^2 \eta & \text{slot} \end{cases}$$

where η is the impedance of free space (376.7 Ω). When these are integrated over the radiation sphere to compute the power radiated, the results contain either $|I_0|^2$ (dipole) or $|V_0|^2$ (slot), the maximum sinusoidal current (voltage). We define the radiation resistance (conductance) as

$$R_r = \frac{P_r}{|I_0|^2} \qquad \text{dipole}$$

$$G_r = \frac{P_r}{|V_0|^2} \qquad \text{slot}$$

(5-4)

Figure 5-4 is a plot of the radiation resistance of each versus length [2, p. 157]. The input resistance differs from the radiation resistance because it is the ratio of the input current (voltage) to the power radiated:

$$I_i = I_0 \sin \frac{kL}{2} \qquad \text{dipole}$$

$$V_i = V_0 \sin \frac{kL}{2} \qquad \text{slot}$$

(5-5)

Combining Eqs. (5-4) and (5-5), we find that

$$R_i = \frac{R_r}{\sin^2(kL/2)} \qquad \text{dipole}$$

$$G_i = \frac{G_r}{\sin^2(kL/2)} \qquad \text{slot}$$
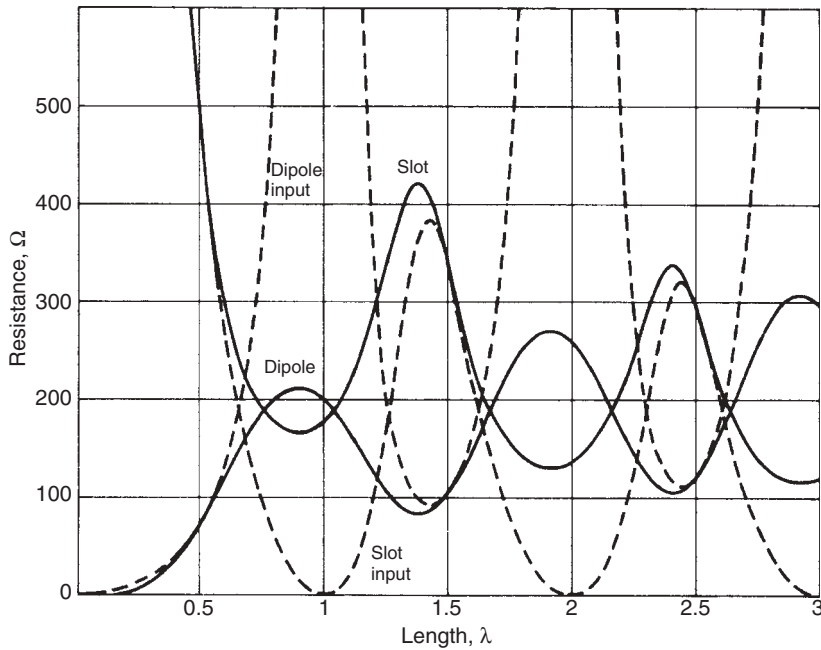
(5-6)

FIGURE 5-4   Dipole and slot radiation and center-fed input resistances.

The input resistances (Figure 5-4) differ from the radiation resistances by Eq. (5-6). The input resistance of a one-wavelength dipole is large but not infinite, as shown; it depends greatly on the diameter and input region. If we take the product of the radiation or input resistances, we determine that

$$R_{\text{dipole}} R_{\text{slot}} = \frac{\eta^2}{4} \tag{5-7}$$

one of the consequences of the Babinet–Booker principle [3].

The input resistance depends on the current at the input [Eq. (5-6)]. When the standing-wave current is high and the voltage is low, the input resistance is moderate. A center-fed half-wavelength dipole has the same input resistance as radiation resistance, since the current maximum occurs as the input. On the other hand, a center-fed half-wavelength slot has a current minimum (voltage maximum) at its input, which gives it high input resistance. When both are a full wavelength long, the dipole standing-wave current is at a minimum and the slot standing-wave current is at a maximum (Figure 5-2). The dipole has a high input resistance and the slot has a low input resistance. We can lower the input resistance by feeding at a high current point, but we may excite a distribution different from that expected.

A short dipole looks like a capacitor at the input. As the length increases, the radiation resistance grows and the capacitance decreases. Just before the length reaches $\lambda/2$, the capacitance becomes zero. The exact length at which the antenna resonates (zero reactance) depends on the diameter of the elements and the input gap. A good starting point is 95% of a half wavelength. Beyond the resonant length, the dipole becomes inductive. The impedance of a thin half-wavelength dipole is $73 + j42.2\,\Omega$, whereas the resonant-length dipole resistance is about $67\,\Omega$. The slot looks like an inductor when short. Think of it as a short-length short-circuited shunt slotline stub. The inductance increases as its length increases and the slot resonates like the dipole, just short of $\lambda/2$. Additional resonances occur at longer lengths. Increasing the frequency is equivalent to increasing the length for the thin dipole.

5-3 BABINET–BOOKER PRINCIPLE [3; 4, p. 337]

A strip dipole and a slot are complementary antennas. The solution for the slot can be found from the solution to an equivalent dipole by an interchange of the electric and magnetic fields. Not only the pattern but also the input impedance can be found. Figure 5-5 shows two such complementary structures. Babinet's principle of optical screens (scalar fields) states that given the solutions to the diffraction patterns of a screen, F_i, and the screen's complement, F_c, the sum equals the pattern without the screen. Booker extended Babinet's principle to vector electromagnetic fields. Strict complementation of an electric conductor requires a nonexistent magnetic conductor. Booker solved this problem by using only perfectly conducting infinitesimally thin screens and by interchanging the electric and magnetic fields between the screen and its complement. If we take two such complementary screens and perform line integrals over identical paths to compute the impedance of each, we obtain the result
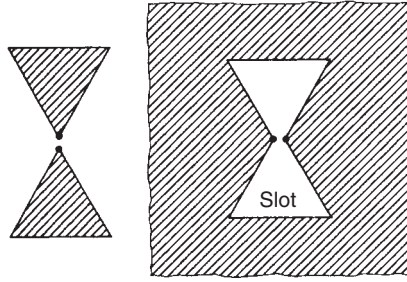
$$Z_1 Z_c = \frac{\eta^2}{4} \tag{5-8}$$

FIGURE 5-5   Complementary screens.

where Z_1 is the input impedance of the structure, Z_c the input impedance of the complementary structure, and η the impedance of free space (376.7 Ω). Equation (5-8) extends Eq. (5-7) to the total impedance and includes mutual impedances as well as self-impedances.

Certain antennas, such as flat spirals, are self-complementary—an exchange of the spaces and conductors leaves the structure unchanged except for rotation. For a two-arm structure,

$$Z_0^2 = \frac{\eta^2}{4} \quad \text{or} \quad Z_0 = 188 \, \Omega$$

Rumsey [5, p. 28] extended these ideas to antennas with more than two conductors to determine the input impedances in various feeding modes.

We must relate flat-strip dipoles to normal round-rod dipoles to use the available results for round dipoles. The diameter of an equivalent round rod equals one-half the strip width of the flat structure. Consider a thin dipole with its near $\lambda/2$ resonance of 67 Ω. We calculate equivalent slot impedance from Eq. (5-8):

$$Z_{\text{slot}} = \frac{376.7^2}{4(67)} = 530 \, \Omega$$

A half-wavelength slot impedance is

$$Z_{\text{slot}} = \frac{376.7^2}{4(73 + j42.5)} = 363 - j211 \, \Omega$$

The $\lambda/2$ dipole is inductive when it is longer than a resonant length, whereas the slot is capacitive.

5-4   DIPOLES LOCATED OVER A GROUND PLANE

We analyze a dipole over a ground plane as a two-element array of the dipole and its image. The ground plane more than doubles the gain of the element by limiting the radiation directions. We can expect a change in the input impedance as the dipole interacts with its image. A vertical dipole excites currents in the ground plane, when transmitting, equivalent to its image. The image is vertical (Figure 5-6) and has the same phase as the dipole (even mode). The impedance of the dipole becomes
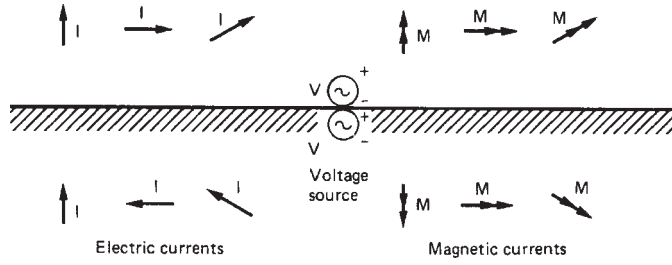
FIGURE 5-6   Ground-plane images.

$Z = Z_{11} + Z_{12}$. Z_{12} is the mutual impedance between the dipole and its image spaced $2H$, where H is the center height of the dipole over the ground plane. The array radiates its maximum in the direction of the ground plane. The dipole also radiates its maximum pattern along the ground plane given by

$$U_{\text{max}} = \frac{\eta |I_0|^2}{(2\pi)^2} \left(1 - \cos \frac{kL}{2} \right)^2 \tag{5-9}$$

where L is the dipole length. The radiated power of the single dipole is

$$P_{\text{in}} = R_{11} |I_0|^2 \left(1 + \frac{R_{12}}{R_{11}} \right)$$

The two-element array increases the field over a single element by 2 and the radiation intensity by 4:

$$\text{directivity} = \frac{4U_{d,\text{max}}}{P_{\text{in}}/4\pi} = \frac{4\eta[1 - \cos(kL/2)]^2}{(R_{11} + R_{12})\pi}$$

We used only the power into the dipole, since no source is connected to the image. Figure 5-7 is a plot of the directivity of a vertical dipole versus height over the ground plane.

A horizontal dipole and its image (Figure 5-6) form an odd-mode two-element array (Section 3-1). The input impedance of the dipole becomes $Z_{11} - Z_{12}$ for the odd-mode array. The value of the mutual impedance Z_{12} approaches that of the self-impedance Z_{11} as the two dipoles move close together. The input impedance approaches zero as the distance from the dipole to ground plane shrinks. The input impedance of all odd-mode array elements decreases as the elements approach each other. The two-element odd-mode array produces a null along the ground plane. The beam peak occurs normal to the ground plane ($\theta = 0°$) when the distance between the dipole and its image is less than $\lambda/2$ or $H \le \lambda/4$. The pattern bifurcates after that height is exceeded. The maximum radiation from the array is

$$U_{A,\text{max}} = \begin{cases} 4 \sin^2 \dfrac{2\pi H}{\lambda} & H \le \dfrac{\lambda}{4} \\ 4 & H \ge \dfrac{\lambda}{4} \qquad \theta_{\text{max}} = \cos^{-1} \dfrac{\lambda}{4H} \end{cases}$$
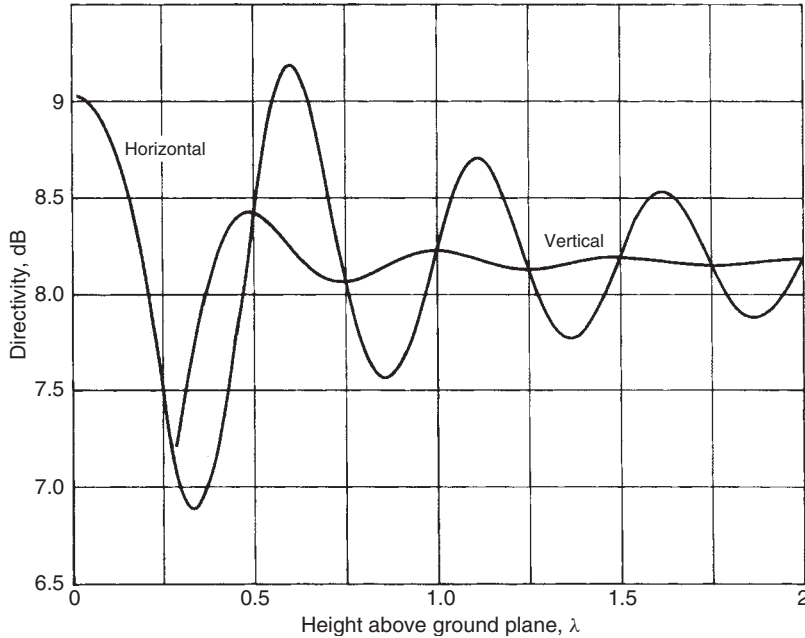
FIGURE 5-7   Directivity of half-wavelength dipoles over a ground plane.

The dipole pattern [Eq. (5-2)] increases the radiation intensity. The total input power into the single dipole becomes

$$P_{in} = |I_0|^2(R_{11} - R_{12})$$

$$\text{directivity} = \frac{U_{A,\max}U_{d,\max}}{P_{in}/4\pi}$$

After inserting the various terms, we obtain the directivity of a horizontal dipole over ground:

$$\text{directivity} = \begin{cases} \dfrac{4\eta \sin^2(2\pi H/\lambda)[1 - \cos(kL/2)]^2}{\pi(R_{11} - R_{12})} & H \le \dfrac{\lambda}{4} \\[4mm] \dfrac{4\eta[1 - \cos(kL/2)]^2}{\pi(R_{11} - R_{12})} & H \ge \dfrac{\lambda}{4} \end{cases}$$

Its plot is included in Figure 5-7.

5-5   DIPOLE MOUNTED OVER FINITE GROUND PLANES

Most configurations have a dipole mounted over a finite ground plane. You can calculate the final pattern by using GTD, PO, or MOM, or you can measure the pattern using the actual ground plane. Analyses produce idealized patterns, and measurements contain errors due to the presence of the positioner mounting. If the final system requires
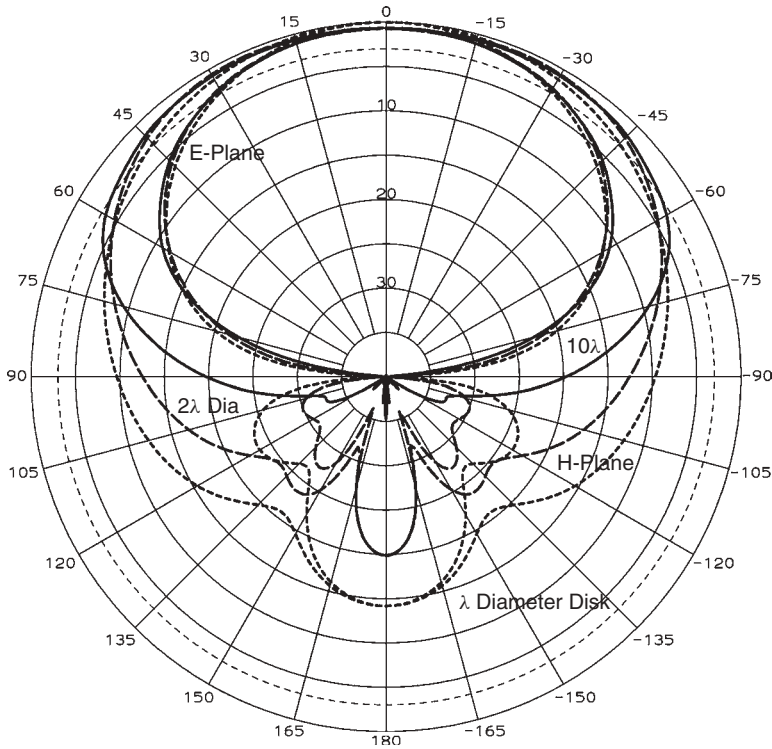
FIGURE 5-8   Dipole spaced $\lambda/4$ over disk ground planes with 1λ, 2λ, and 10λ diameters.

exacting patterns, it has no margin and will fail. In this section we consider dipoles with idealized ground planes and give you ideas about the final performance or spur you to use the ground plane purposely as a design parameter.

Figure 5-8 shows the result of a PO analysis of a dipole mounted $\lambda/4$ above finite disks 1, 2, and 10λ in diameter. The E-plane pattern contains a pattern null at $90°$ due to the dipole pattern. The ground plane restricts the broad H-plane pattern as pattern angles approach $90°$ and reduces the backlobe more and more as it increases in size. At one wavelength the disk increases the gain of the antenna from the $7.5\,\text{dB}$ given in Figure 5-7 to $8.1\,\text{dB}$. We can size the ground plane to produce small gain increases.

We can analyze flat-plate reflectors from three perspectives. In the first, plates restrict radiation directions and thereby increase directivity. Waves polarized parallel with the surface must vanish on the reflector surface and cause a greater restriction of the beam. We see this effect in Figure 5-7, which shows horizontal dipoles having greater directivities than vertical dipoles for close spacing over a ground plane. In the second method we use aperture theory to analyze the reflector by using an aperture plane and integrate the fields or evaluate illumination losses. If the phase of the fields on the aperture varies rapidly, we must either take fine increments in numerical integration or evaluate only around areas of stationary phase. Third, we can replace the reflector with images and restrict the valid pattern region. In GTD this method is combined with diffractions to smooth the field across shadow and reflection boundaries.

In Section 5-4 we analyzed the pattern and gain of a dipole mounted over an infinite ground plane by the method of images. The antenna and its image formed a two-element

TABLE 5-1   Results of a GTD Analysis of a Horizontal $\lambda/2$ Dipole $\lambda/4$ Over a Limited Square Ground Plane (H-Plane)

Ground-Plane Size (λ)	Directivity (dB)	Front-to-Back Ratio (dB)	H-Plane Pattern Level at 90° (dB)	H-Plane Beamwidth (deg)	Phase Center (λ)
0.5	5.37	8.4	−6.3	108.5	0.18
0.6	6.32	10.3	−7.6	104.0	0.15
0.7	7.08	12.0	−8.8	100.9	0.14
0.8	7.68	13.5	−9.8	97.8	0.12
0.9	8.14	14.8	−10.6	95.1	0.10
1.0	8.34	16.0	−11.2	93.2	0.08
1.2	8.65	17.8	−12.0	93.3	0.04
1.4	8.45	19.1	−12.3	99.4	0.01
1.6	7.96	20.0	−12.2	108.4	0.0
1.8	7.39	21.1	−12.3	112.4	0.0
2.0	6.95	22.3	−12.4	113.1	0.0
2.5	7.13	25.0	−12.7	115.8	0.0
3.0	7.74	28.3	−13.8	111.4	0.0
4.0	7.28	32.8	−14.8	116.1	0.0
5.0	7.56	35.4	−16.2	118.0	0.0
10	7.41	36	−19.1	121.3	0.0

array, but with real power into only one element. The imaging method gives limited information that can be filled with GTD methods. Table 5-1 lists the results of a GTD analysis of a half-wavelength horizontal dipole located $\lambda/4$ over a limited square ground plane. An infinite ground plane and dipole combination has an infinite front-to-back (F/B) ratio with the fields vanishing in the ground-plane direction. By using the methods of Section 3-3, we calculate a 120° half-power beamwidth for the two-element half-wavelength spaced array of the dipole and its image. The F/B ratio increases as the reflector (ground plane) size increases. Unfortunately, F/B is only the ratio of two pattern angles. We could tune the size of the ground plane to produce a high F/B ratio for a nonsquare ground plane, but it holds for only a small range of angles. Figure 5-8 illustrates the general increase in F/B as the size of the ground plane increases. We expect zero fields at $\theta = 90°$ on an infinite ground plane, and Table 5-1 shows a decrease of the fields with an increase of the ground plane. The half-power beamwidth cycles about 120° as the ground plane increases in size.

Phase center is the apparent radiation center placed at the focus of a paraboloidal reflector when used as a feed. The phase center of the equivalent two-element array is located on the ground plane. As we decrease the ground plane, the effect of the image decreases and causes the phase center to move toward the dipole. In the limit of no ground plane, the phase center is on the dipole.

Table 5-1 shows the small gain changes that occur as the relative phase of the ground-plane scattered fields and the dipole direct fields add in the far field. The small ground plane at $\lambda/2$ square fails to significantly limit radiation and gain drops. Peak gain occurs when the ground plane is 1.2λ square, but this result would not necessarily hold for a circular ground plane. In most applications the dipole cannot be mounted directly above the ground-plane center, but we can add a small ground plane to control
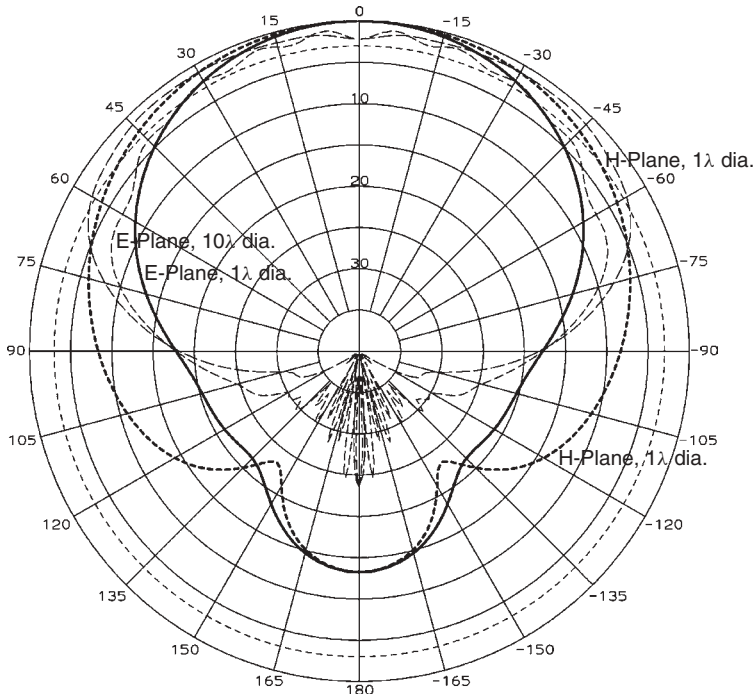
FIGURE 5-9   V-dipole spaced 0.35λ over and tilted 35° toward 1λ- and 10λ-diameter ground planes.

the pattern and then place the combination on a pedestal over the larger ground plane. Most cases should be analyzed or measured in the final configuration.

The dipole E-plane pattern null can be reduced by tilting the two poles down toward the ground plane. Figure 5-9 illustrates the calculated pattern of a tilted element dipole above a finite disk ground plane. The feed point of the dipole has been raised to 0.35λ to allow for the 35° tilt to the poles. Tilt and ground-plane height give additional parameters to control the pattern of the dipole mounted over a finite ground plane. For example, a horizontal dipole located λ/2 over an infinite ground plane forms an odd-mode (0°, 180°) two-element array using the dipole and its image. The simple ray-tracing argument given in Section 3-1 predicts a pattern null at zenith. But when placed over a finite ground plane, the fainter image fails to produce a complete null.

We sometimes mount a dipole spaced away from a metal cylinder that provides a ground plane to restrict radiation. The curved ground plane allows greater radiation around the cylinder when rays spread as they scatter from it. Figure 5-10 shows the horizontal plane pattern for a vertical dipole mounted near a 1λ-diameter cylinder for spacing of 0.25λ, 0.4λ, 0.5λ, and 0.75λ. When we space a dipole λ/2 above a large flat ground plane, the pattern has a null normal to the plane. The cylinder is unable to generate a full image of the dipole to produce this null, but the pattern does dip 11.2 dB from the peak. A dipole spaced 3λ/4 over a ground plane produces a three-lobed pattern that we can see in Figure 5-10 except that the cylinder can produce only 8-dB dips. If we mount the dipole over a 2λ-diameter cylinder, the pattern is similar to Figure 5-10 except that F/B increases and the nulls have greater depths. Table 5-2 summarizes pattern results for vertical dipoles mounted over small cylinders.
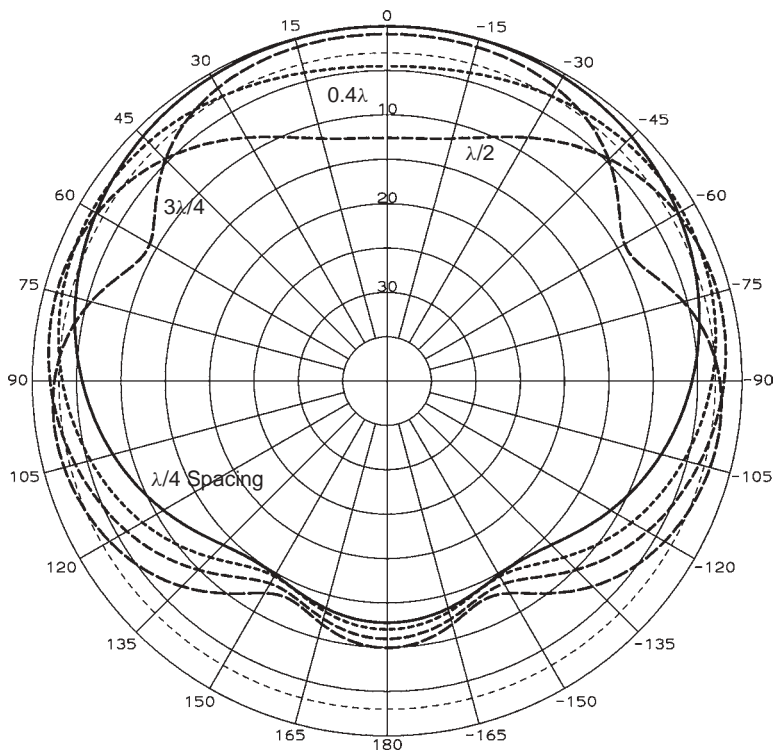
FIGURE 5-10 Horizontal plane pattern for a vertical dipole mounted near a 1λ-diameter cylinder at 0.25λ, 0.4λ, 0.5λ, and 0.75λ distances.

TABLE 5-2   Dipole Mounted Over a Cylinder Aligned with a Cylinder

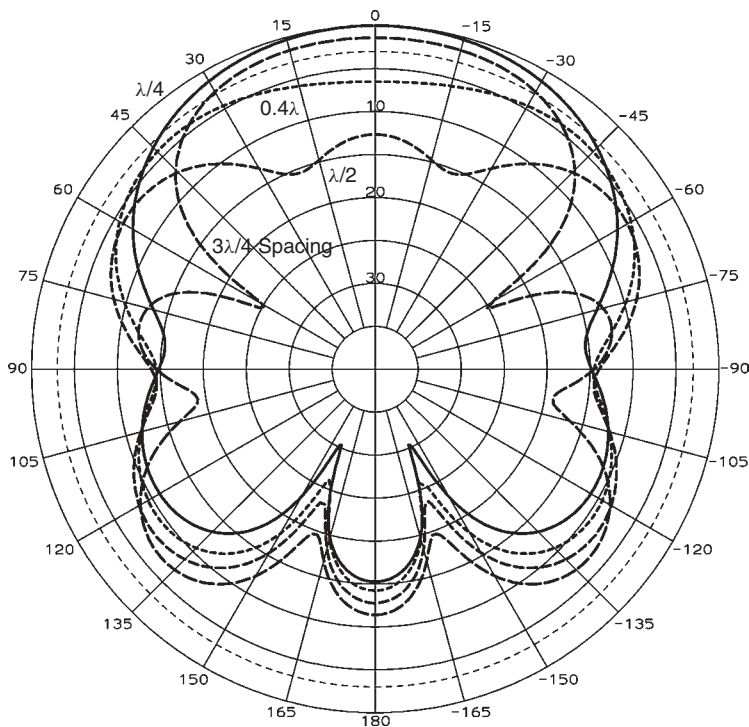| Height (λ) Over Cylinder	Cylinder Diameter (λ)	Gain (dB) At 0°	Gain (dB) At 180°	Gain Peak	Peak Angle
0.25	0.25	3.5	−2.1	3.6	0
	0.50	6.1	−2.7	6.1	0
	1.0	6.7	−6.1	6.7	0
	2.0	7.3	−10.7	7.3	0
0.4	0.25	3.2	0.3	4.9	64
	0.50	3.6	−1.3	6.0	62
	1.0	2.2	−5.3	5.1	60
	2.0	2.2	−9.7	6.0	54
0.5	0.25	0.5	0.9	5.2	80
	0.50	−2.9	−1.8	4.8	80
	1.0	−5.9	−4.2	5.2	76
	2.0	−8.7	−8.5	5.9	70
0.75	0.25	3.3	−0.2	3.4	102
	0.50	5.0	−0.9	4.7	102
	1.0	5.1	−3.2	4.6	98
	2.0	6.4	−6.8	5.2	90

FIGURE 5-11 Horizontal dipole mounted over a vertical 1λ diameter pole at 0.25λ, 0.4λ, 0.5λ, and 0.75λ distances.

TABLE 5-3   Dipole Mounted Over a Cylinder Perpendicular to a Cylinder

Height (λ) Over Cylinder	Cylinder Diameter (λ)	Gain (dB) At 0°	At 180°	Gain Peak Perpendicular to Plane	Peak Angle Perpendicular to Plane
0.25	0.25	3.8	−2.6	3.8	0
	0.50	6.6	−4.4	6.6	0
	1.0	7.1	−8.2	7.1	0
	2.0	7.0	−8.6	7.4	30
0.4	0.25	3.0	−0.2	4.9	46
	0.50	2.9	−2.5	6.5	48
	1.0	0.6	−7.1	6.4	50
	2.0	1.2	−7.3	7.3	54
0.5	0.25	0.0	0.5	5.1	54
	0.50	−4.2	−2.8	5.2	54
	1.0	−5.6	−5.7	6.6	56
	2.0	−6.7	−6.3	7.3	60
0.75	0.25	3.5	−0.4	2.7	66
	0.50	5.3	−1.6	4.3	66
	1.0	5.7	−4.3	5.1	66
	2.0	6.4	−5.7	5.8	70

To complete the analysis, the dipole was rotated so that its axis is perpendicular to the pole. Figure 5-11 illustrates the patterns calculated for a horizontally polarized dipole mounted above a vertical pole. We expect a pattern null at 90° in this horizontal plane due to the dipole polarization null, but the dipole induces curved currents on the cylinder that radiate and fill in these nulls. The null due to the dipole does narrow the pattern in the horizontal plane compared to Figure 5-10, and in many cases peak radiation occurs in the vertical plane. Table 5-3 lists the characteristics of the horizontal dipole mounted over a vertical pole for various dipole spacing above the pole and its diameter.

5-6   CROSSED DIPOLES FOR CIRCULAR POLARIZATION

We produce a circularly polarized antenna by placing two dipoles along the x- and y-axes over a ground plane and feeding them with equal amplitudes and quadrature phase (0° and −90° for RHC). Without the ground plane the combination radiates LHC in the −z direction. The ground plane changes the sense of circular polarization of the wave radiated in the −z-direction and it adds with the direct radiated wave. The dipoles are fed from either dual folded baluns that produce two separate inputs or by a split coax balun connecting both dipoles in shunt. The shunt connection requires differing lengths for the dipoles to produce the 90° phase difference that we call the *turnstile configuration*.

The dual-feed antenna uses either a quadrature hybrid equal-amplitude power divider to feed the two ports or an equal phase and amplitude power divider with an extra line length on one of the two ports. The hybrid power divider feed produces an antenna with a wide impedance and axial ratio bandwidth. The hybrid power divider has two inputs that provide ports for both RHC and LHC polarizations. The signals reflected from the two equal-length dipoles when fed from one port of the hybrid reflect into the second port due to the phasing in the hybrid coupler. When measuring at one port of the hybrid, the impedance bandwidth is quite broad because the reflected power is dissipated in the load on the other port. This dissipated power lowers the efficiency of the antenna, a hidden loss unless you measure the coupling between the inputs of the hybrid. The second configuration, using the extra line length, produces an antenna with a narrowed axial ratio bandwidth and a wider impedance bandwidth compared to a single dipole. The extra 180° round-trip total signal path in one arm causes the equal reflections to cancel. Figure 5-12 gives the circularly polarized pattern from a pair of crossed dipoles over a ground plane with a perfect feed. The E-plane dipole null limits the angular range of good circular polarization. We improve the circular polarization by raising the dipoles a little and tilting them down to widen the E-plane beamwidth. Figure 5-12 shows the pattern for the tilted dipole pair and illustrates the improved cross polarization and the wider beamwidth. The placement on a finite ground plane complicates this result somewhat and will require extra design effort.

Turnstile feeding exploits the impedance properties of the dipole to shift the relative phase between two different dipoles when shunt connected to the same port. When we shorten a dipole below resonance, its impedance is capacitive and its current has positive phase relative to the resonant-length dipole, while the lengthened dipole has an inductive reactance and a negatively phased current. We determine the lengths of
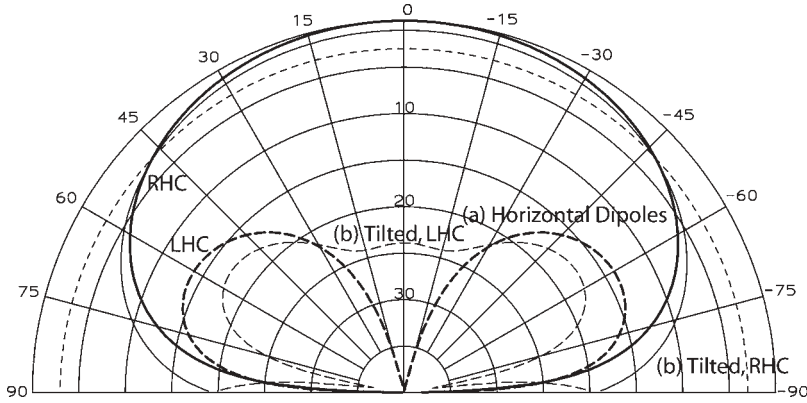
FIGURE 5-12   Crossed dipoles fed for circular polarization: (*a*) $\lambda/4$ height and $0°$ tilt; (*b*) 0.3λ height and $30°$ tilt.

the two dipoles by a perturbation technique using the Q of the resonant circuit of the dipole. Q is related to the VSWR bandwidth:

$$\text{BW} = \frac{\text{VSWR} - 1}{Q\sqrt{\text{VSWR}}} \qquad Q = \frac{\text{VSWR} - 1}{\text{BW}\sqrt{\text{VSWR}}} \qquad (5\text{-}10)$$

We derive the lengths of the two dipoles in terms of the resonant (zero reactance)-length dipole, L_0:

$$L_x = \frac{L_0}{\sqrt{1 + 1/Q}} \qquad L_y = L_0\sqrt{1 + \frac{1}{Q}} \qquad \text{RHC polarization} \qquad (5\text{-}11)$$

A dipole of 0.014λ diameter located 0.3λ above a ground plane and tilted down $30°$ has a resonant length of 0.449λ. The $2:1$ VSWR bandwidth for $70\,\Omega$ is 18.3% or a Q of 3.863 by using Eq. (5-10). When we insert this Q in Eq. (5-11), we calculate the two lengths for a turnstile design: $L_x = 0.400\lambda$ and $L_y = 0.504\lambda$ for RHC polarization. The $+x$ and $+y$ poles are fed from the same port. Figure 5-13 plots the Smith chart of this design. The trace on a Smith chart rotates clockwise for increasing frequency. The cusp in the trace is the frequency with the best axial ratio, which did not occur at the frequency of best match. Nevertheless, the $2:1$ VSWR bandwidth of the antenna has increased to 41.5% because the combined reactance of the two dipoles cancels over a large frequency range. At center frequency the pattern is similar to Figure 5-12 except that the patterns in the two planes have slightly different beamwidths due to the dipole lengths. When the frequency shifts off center, the axial ratio degrades. The axial ratio bandwidth is far less than the impedance bandwidth, and the design gives a 16.4% 6-dB axial ratio bandwidth. An axial ratio of $6\,\text{dB}$ produces 0.5-dB polarization loss similar to the $0.5\,\text{dB}$ reflected power loss of $2:1$ VSWR. This illustrates the importance of considering not only the impedance bandwidth but also the pattern characteristics over the frequency band.

We can increase the beamwidth of the turnstile dipole located over a ground plane by adding a notched cone under it. Figure 5-14 illustrates the arrangement of the slightly
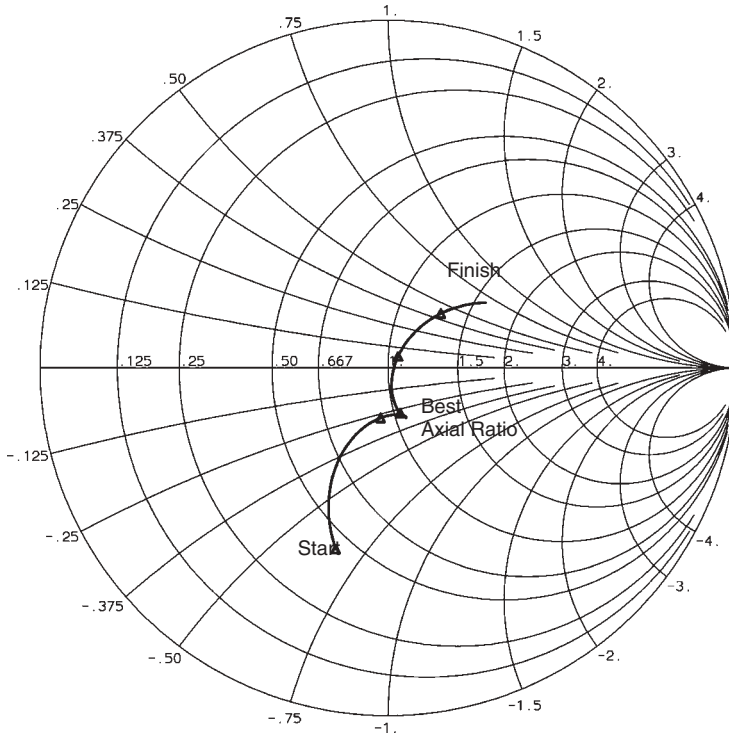
FIGURE 5-13   Smith chart response of a turnstile dipole pair $L_x = 0.400\lambda$ and $L_y = 0.504\lambda$ mounted 0.30λ over a ground plane with $30°$ tilt.
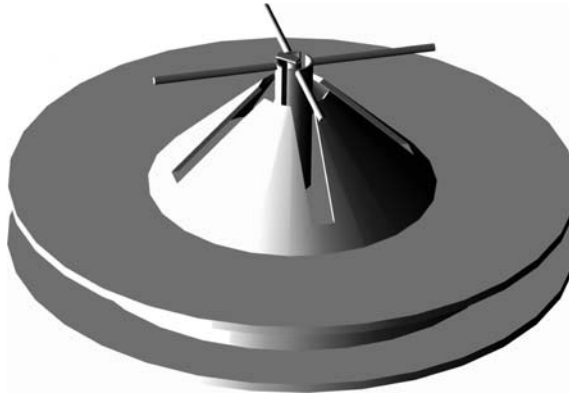

FIGURE 5-14   Turnstile dipole mounted over a notched cone on a finite circular ground plane with radial line chokes to reduce the backlobe.

less than $\lambda/4$-long notches in a $45°$ cone with the turnstile dipoles located about $\lambda/4$ above the ground plane. A split-tube coaxial balun feeds the two dipoles sized as a turnstile with dipoles of longer and shorter length. The upper feed jumper excites RHC radiation. The dipoles excite magnetic currents in the slots that radiate a broad pattern to fill in the E-plane nulls of the dipoles. On an infinite ground plane the horizontal
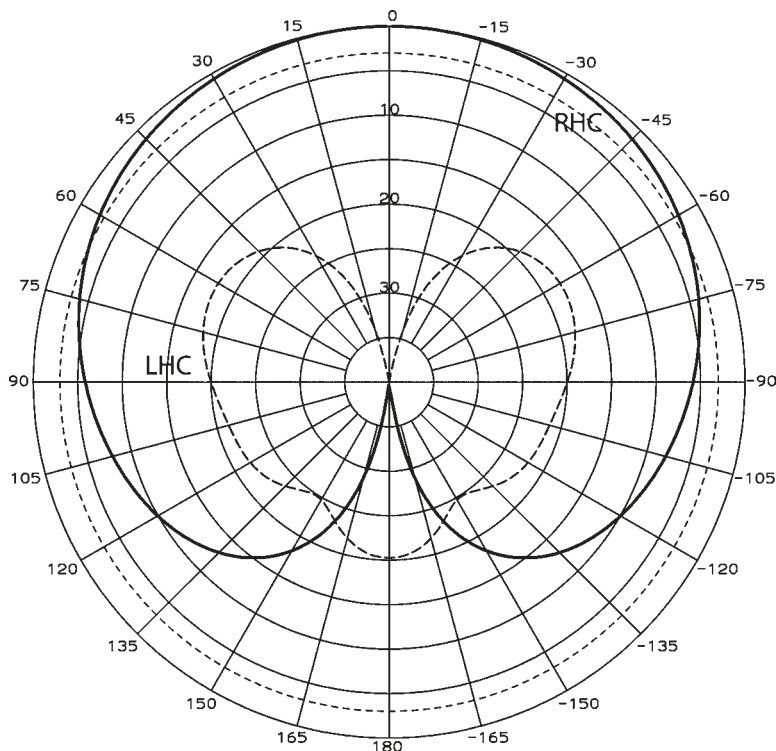
FIGURE 5-15   Pattern of a turnstile dipole mounted over a notched cone with a 0.75λ ground plane and two radial chokes.

polarization must vanish along the ground plane, and the RHC and LHC components would be equal at 90° similar to the pattern shown in Figure 5-12. By using a finite-size ground plane, the horizontal component does not vanish, and a wide beamwidth is obtained with circular polarization at 90° as shown in Figure 5-15, which uses a 0.75λ-diameter ground plane and 0.5λ-base-diameter cone. To reduce the backlobe below the ground plane, two short-circuited radial transmission line chokes were placed around the edge to form a soft surface. We size the inner radius so that the transmission line produces an open-circuit impedance at the outer rim that reduces the edge diffraction and the backlobe [6, p. 88]. From a PO perspective the radial line choke is a slot that supports a magnetic current loop. This example illustrates that slots or notches can be used to shape the patterns of small antennas.

5-7   SUPER TURNSTILE OR BATWING ANTENNA [7]

The super turnstile or batwing antenna was developed for TV transmitter antennas. The antenna combines a slot with a dipole batwing to produce an antenna with a wide impedance bandwidth. Figure 5-16 shows the normal configuration, with four wings placed around a central support metal mast. Each wing connects to the mast at the top and bottom with a metal-to-metal connection. The inner vertical rod and the support
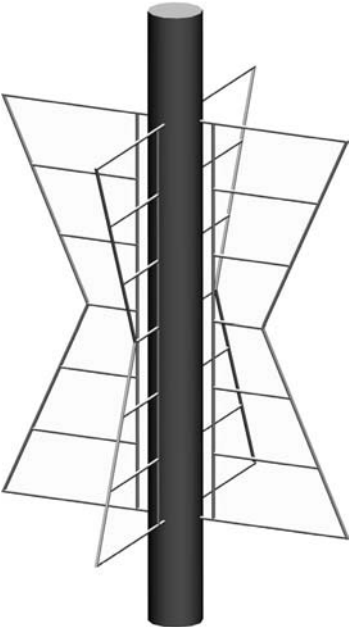
FIGURE 5-16   Super turnstile or batwing antenna using an open rod construction.
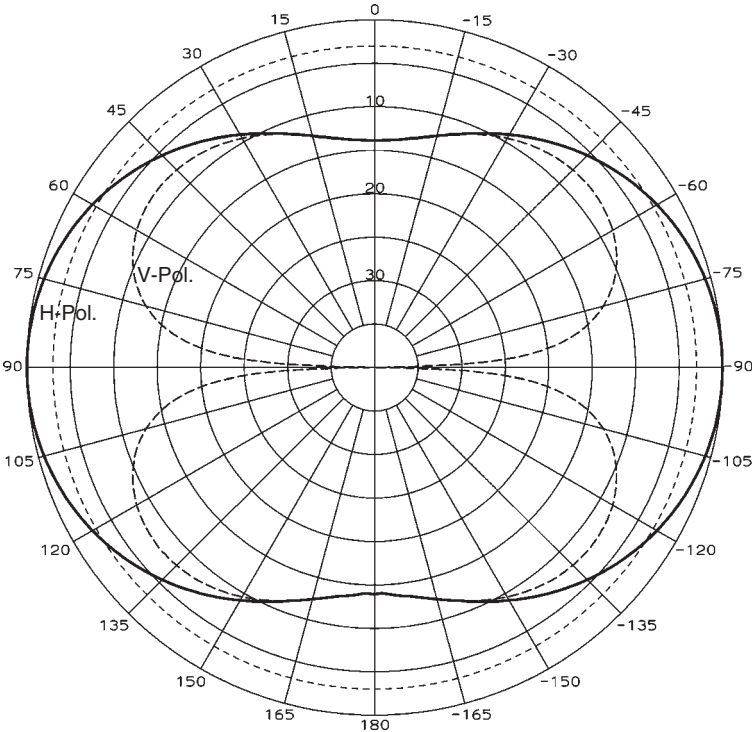

FIGURE 5-17   Elevation pattern of a single bay of a super turnstile antenna showing horizontal and vertical polarization components.

mast form a two-line slot fed by a jumper located at the center of each wing. To produce an omnidirectional pattern about the mast, a feed power divider located inside the mast phases the inputs for circular polarization (0°, 90°, 180°, 270°). The antenna radiates horizontal polarization in the horizontal plane but radiates cross-polarization that increases with elevation (depression) angle as shown in Figure 5-17. A four-wing antenna produces a horizontal plane pattern ripple of about 1.5 dB. Adding more wing antennas around a larger central mast reduces the ripple.

The extraordinary characteristic of the antenna is its impedance bandwidth. Figure 5-18 gives the return loss frequency response for a wire frame antenna. The 1.1 : 1 VSWR bandwidth is about 35%; if adjusted to 1.25 : 1 VSWR, the antenna has a 51% bandwidth. You make small adjustments to the spacing between the mast and the inner rod to tune the VSWR. Table 5-4 lists the parameters of batwing antennas with both wire frame and solid panel wings. The solid panels lower the input impedance to 75 Ω from the 100 Ω of the wire frame antenna. Using an antenna with only two wings
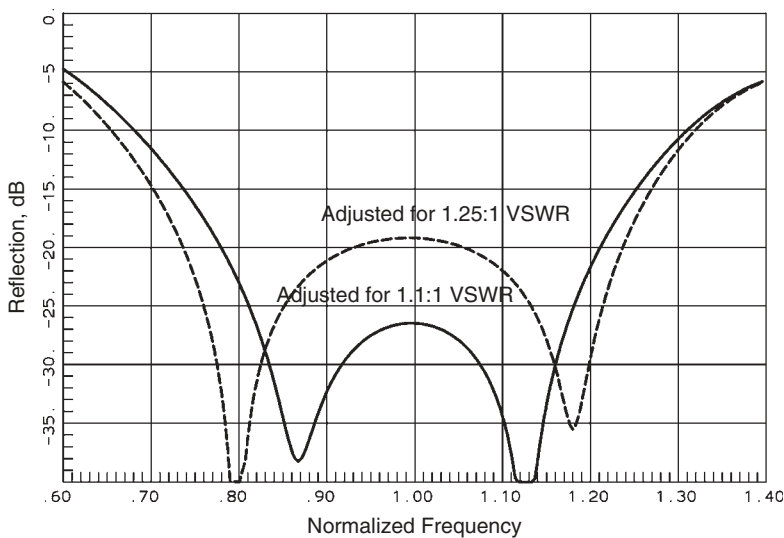

FIGURE 5-18   Super turnstile wire frame antenna return-loss response adjusted for 1.1 : 1 and 1.25 : 1 VSWR.

TABLE 5-4   Dimensions of a Super Turnstile Antenna in Wavelengths for Four Wings Center-Fed for Circular Polarization

Parameter	Wire Frame	Solid Wing
Impedance (Ω)	100	75
Height	0.637	0.637
Wing upper	0.2254	0.229
Wing middle	0.0830	0.0847
Gap	0.0169	0.0216
Rod diameter	0.0508	
Mast diameter	0.0847	0.0847

changes the input impedance from the value for an antenna with four wings because the close coupling between the wings alters the impedance. It depends on the feeding mode. This holds for any antenna with close coupling: for example, a spiral antenna. You must feed it in the operating mode to measure the correct input impedance. The transmitter antenna will consist of a number of these antennas stacked vertically to produce a narrow pattern directed at the horizon.

5-8   CORNER REFLECTOR [8, p. 328]

The usual corner reflector (Figure 5-19) has a dipole located between two flat plates that limit directions of radiation. The angle between the reflectors can be any value, but $90°$ seems to be the most effective. On paper, decreased angles give better results, but only marginally. We could consider the flat plate as a limiting case. The tangential electric fields must vanish at the surface of the flat plates. We discover a greater restriction, since the fields can only decrease gradually in the limited space between the ground planes and the dipole. Most of the power is concentrated in lower-order spherical modes. In the limit of zero vertex distance, the single mode possible restricts the beamwidth to $45°$ in the H-plane.

We analyze the $90°$ corner reflector as an array by using the three images of the dipole in the ground planes (Figure 5-19) plus the real dipole. The array factor of the array of dipole and images is

$$\left| e^{jkd\cos\theta} + e^{-jkd\cos\theta} - (e^{jkd\sin\theta\sin\phi} + e^{-jkd\sin\theta\sin\phi}) \right|^2$$

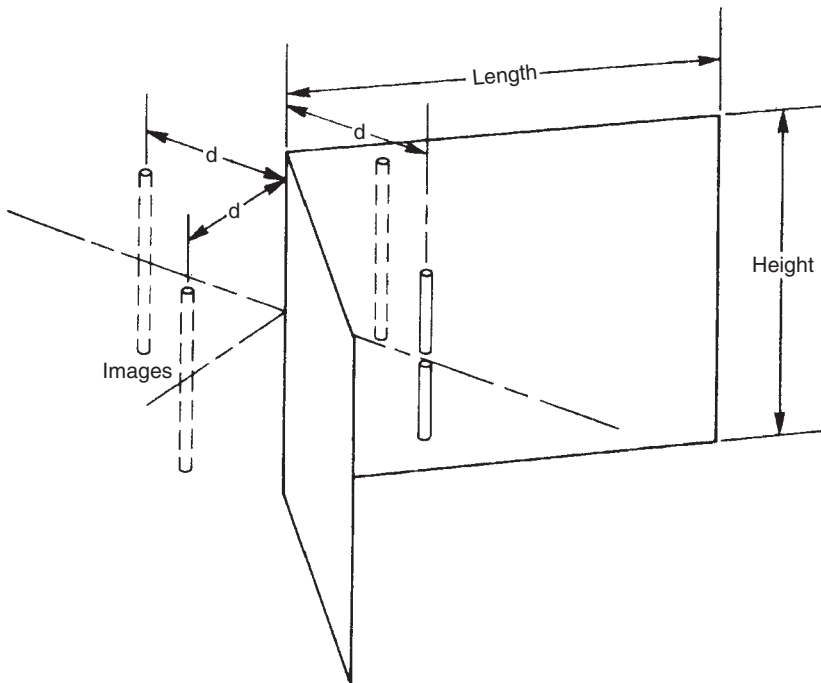**FIGURE 5-19**   A $90°$ corner reflector.

In the H-plane, $\phi = 90°$ and we evaluate terms to get

$$4[\cos(kd\cos\theta) - \cos(kd\sin\theta)]^2$$

where d is the distance from the vertex to the dipole and θ is the H-plane pattern angle from the axis. We must multiply this by the pattern of the dipole to obtain the radiation intensity. We consider only the H-plane, where the maximum radiation intensity is found from Eq. (5-9):

$$U = 4[\cos(kd\cos\theta) - \cos(kd\sin\theta)]^2 \frac{\eta|I_0|^2}{(2\pi)^2}\left(1 - \cos\frac{kL}{2}\right)^2 \qquad (5\text{-}12)$$

where η is the impedance of free space, I_0 the dipole current, and L the dipole length.
   The radiated power of the single dipole is

$$P_{\text{in}} = |I_0|^2[R_{11} + R_{12}(2d) - 2R_{12}(\sqrt{2}\,d)] \qquad (5\text{-}13)$$

where R_{11} is the self-resistance of the dipole and $R_{12}(x)$ is the mutual resistance function between the dipole and its images. The directivity is found from

$$\text{directivity}(\theta) = \frac{4\pi U(\theta)}{P_{\text{in}}} \qquad (5\text{-}14)$$

We combine Eqs. (5-12) and (5-13) into Eq. (5-14) to compute directivity of the 90° corner reflector with infinite sides:

$$\text{directivity}(\theta) = \frac{4\eta[1 - \cos(kL/2)]^2[\cos(kd\cos\theta) - \cos(kd\sin\theta)]^2}{R_{11} + R_{12}(2d) - 2R_{12}(\sqrt{2}\,d)} \qquad (5\text{-}15)$$

Table 5-5 gives the directivity, beamwidth, and impedance of a 90° corner reflector fed from a dipole 0.42λ long and 0.02λ in diameter. We must shorten the dipole further than a free-space dipole length at resonance to compensate for the mutual coupling between dipoles. Directivity increases as the vertex distance decreases, but the effects of superdirectivity cause the efficiency and gain to fall as the vertex is approached. The antenna has a 50-Ω input impedance for $d = 0.37λ$. This point shifts when we increase the dipole's diameter to increase its bandwidth.
   Kraus gives the following guidelines for the size of the sides. Each plate should be at least twice the length of the dipole-to-vertex distance, and the plate height (the dipole direction) should be at least 0.6λ. To evaluate those guidelines, a GTD analysis was performed on various combinations (Table 5-6) with $d = 0.37λ$. The H-plane beamwidth decreases with an increase in plate length. After about 1.5λ sides, the H-plane beamwidth fluctuates about 45° as the sides increase. Even with 5λ sides the beamwidth is below 45°. The E-plane beamwidth fluctuates with the plate height. The directivity was estimated from the beamwidths. In one case—1.5λ sides and 1.5λ high—the estimated directivity exceeds the directivity of the infinite-side case. The edge diffractions add to the reflected and direct radiation of the rest of the antenna.
   Refer to Section 2-4.2 for an example using PO to analyze a corner reflector. Similar to infinite plate analysis, the reaction of the image dipoles in the finite plates can be used to find the input impedance and gain of the antenna. When we analyze the corner

TABLE 5-5   Characteristics of a 90° Corner Reflector with Infinite Sides and 0.42λ Dipole

Vertex Distance (λ)	Directivity (dB)	Beamwidth (deg)	Input Impedance (Ω)
0.30	12.0	44.7	$29.1 - j1.1$
0.32	12.0	44.6	$34.9 + j0.4$
0.34	11.9	44.5	$40.9 + j1.1$
0.36	11.9	44.3	$47.0 + j0.8$
0.37	11.9	44.2	$50.0 + j0.3$
0.38	11.8	44.1	$53.0 - j0.5$
0.40	11.8	43.9	$58.8 - j2.8$
0.42	11.7	43.6	$64.1 - j6.0$
0.44	11.7	43.3	$68.8 - j10.0$
0.46	11.6	42.9	$72.7 - j14.9$
0.48	11.5	42.4	$75.7 - j20.3$
0.50	11.4	41.8	$77.7 - j26.2$
0.52	11.4	41.1	$78.6 - j32.2$
0.54	11.3	40.2	$78.4 - j38.4$
0.56	11.2	39.2	$77.0 - j44.3$
0.58	11.1	38.1	$74.6 - j49.8$
0.60	10.9	36.8	$71.3 - j54.8$

TABLE 5-6   Results of a GTD Analysis of a 90° Corner Reflector with Finite Sides and Vertex Distance 0.37λ

Side Length (λ)	Plate Height (λ)	Beamwidth		F/B (dB)	Estimated Directivity (dB)
		E-Plane	H-Plane		
0.75	0.75	70.4	97.4	18.4	7.7
1.00	0.75	73.6	72.4	17.3	8.8
1.50	0.75	72.6	50.8	18.2	10.0
0.75	1.00	60.2	91.6	23.4	8.5
1.00	1.00	61.0	62.8	22.7	10.1
1.50	1.00	58.5	46.0	23.8	11.4
0.75	1.50	53.4	81.6	34.0	9.3
1.00	1.50	51.6	60.0	39.0	11.0
1.50	1.50	48.2	42.6	46.3	12.6
5.00	5.00	68.8	43.4	63.5	10.8

reflector using GTD, the method does not determine input impedance and gain must be estimated from the patterns. We can use the method of moments to analyze the corner reflector. One preferred construction method is to use rods for the reflector so that the antenna has minimum wind loading. Figure 5-20 illustrates a corner reflector made with only six rods on each side. Figure 5-21 gives the pattern of this antenna from a moment method calculation. This small antenna produces excellent results.

We can use the angle of the sides as a design parameter. A geometric optics analysis that uses images restricts the angle, but nothing stops the antenna from working for
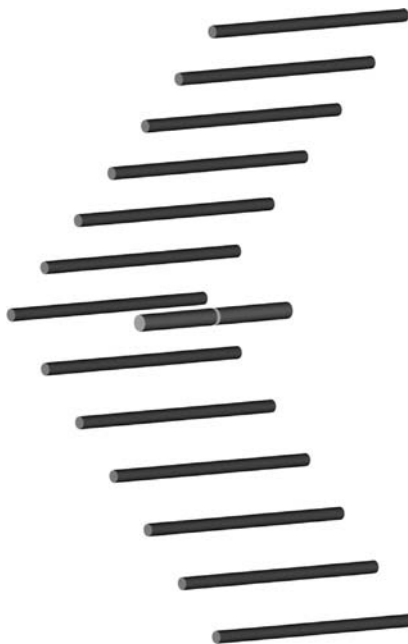
FIGURE 5-20 Corner reflector constructed from 0.6λ-long rods spaced 1/6λ with a dipole spaced 0.37λ from the vertex.

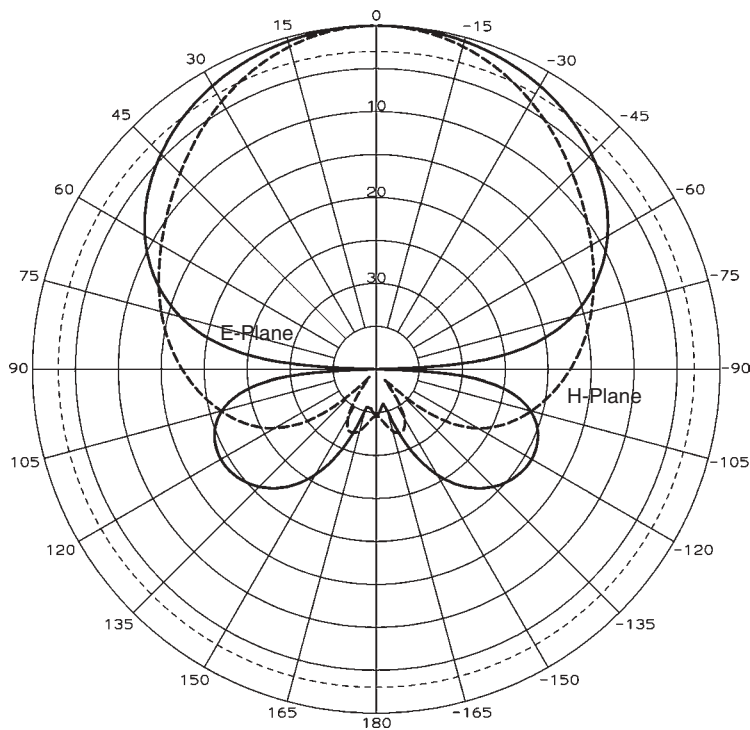**FIGURE 5-21** Pattern of a corner reflector made from 0.6λ-long rods spaced 1/6λ with dipole 0.37λ from vertex.

TABLE 5-7   Corner Reflector with Varying Angle H-Plane 0.9λ-Wide Plates Connected to a 0.2λ Central Plate, 1λ E-Plane Width, Dipole 0.3λ Above the Central Plate

Side Angle	Beamwidth		Gain (dB)	F/B (dB)	Side Angle	Beamwidth		Gain (dB)	F/B (dB)
	E-Plane	H-Plane				E-Plane	H-Plane		
60	58.1	59.4	9.1	21.7	15	59.2	65.9	9.5	19.3
55	57.1	56.0	9.9	22.6	10	61.6	83.3	8.7	26.3
50	56.3	52.3	10.5	23.0	5	64.7	99.2	7.8	25.1
45	55.8	49.1	10.8	23.4	0	67.8	108.6	7.5	23.6
40	55.4	46.8	11.1	22.8	−5	70.2	117.0	7.2	22.0
35	55.4	45.5	11.2	24.3	−10	71.5	125.8	6.9	16.5
30	55.6	45.6	11.0	24.9	−15	71.8	135	6.6	19.0
25	56.2	47.9	10.7	25.5	−20	71.7	143.8	6.3	17.8
20	57.4	53.7	10.2	20.3	−25	71.8	152.2	5.4	16.1
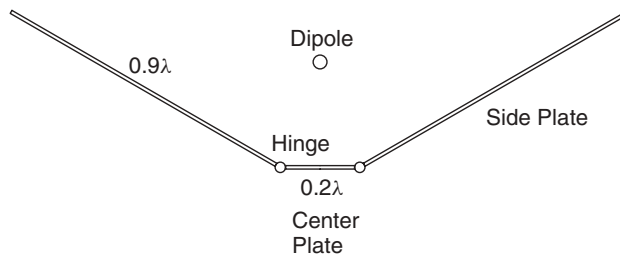
FIGURE 5-22   Corner reflector with variable-angle side plates and a center flat plate.

arbitrary side angles. It is convenient to have a small plate between the tilted sides for the mounting brackets, and these side plates could be mounted on hinges and rotated to vary the H-plane beamwidth. Table 5-7 lists the parameters of a corner reflector 1λ along the E-plane, a central plate 0.2λ wide in the H-plane, and sides 0.9λ long where the side angle is varied. The dipole is located 0.3λ above the central plate. We measure the side plate angle from the plane containing the small central ground plane; zero corresponds to a flat plane ground plane and 45° the usual corner reflector. Negative side-plate angle means that the side plates are tilted behind the central plate away from the dipole. Figure 5-22 illustrates the H-plane cross section of this corner reflector with 30° side plates.

We should not design corner reflectors with large sides since the gain is limited. The gain of paraboloid reflectors of the same size soon exceeds that of a corner reflector. A 2λ-diameter paraboloid reflector at 50% efficiency has a gain of 13 dB, and its gain exceeds that of a corner reflector. Any corner reflector with a vertex angle given by 180°/N, where N is an integer, can be analyzed by the method of images. Corner reflectors with N greater than 2 have only marginally higher gains. The 90° corner reflector gives the best result for a given amount of material. Elkamchouchi [9] adds a cylindrical surface between the plates centered on the vertex. This surface adds another set of images within the cylinder. The images increase the gain by about 2 dB and decrease the frequency dependence of the impedance.
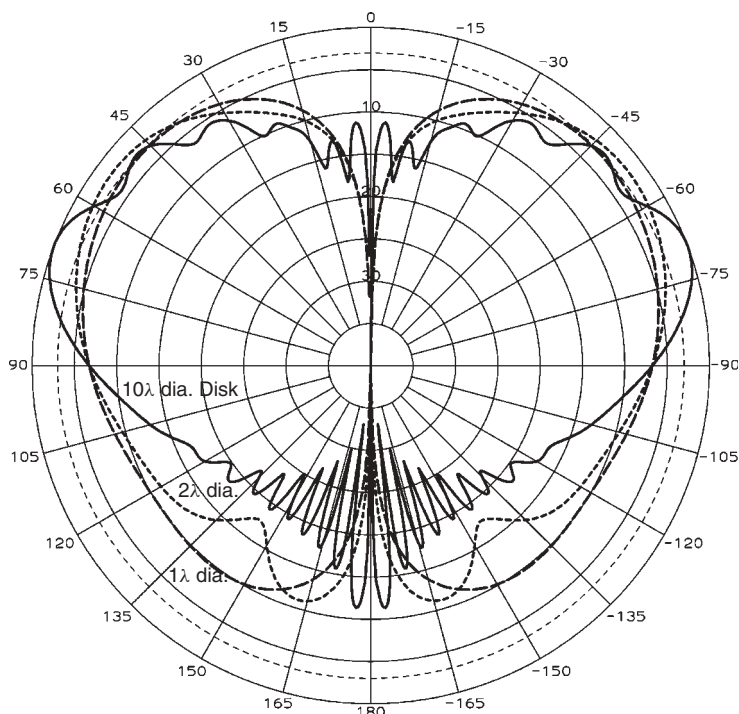
FIGURE 5-23   A $\lambda/4$ monopole located on 1λ-, 2λ-, and 10λ-diameter disk ground planes.

5-9   MONOPOLE

A monopole consists of a single conductor fed out of a ground plane from the center conductor of a coax. When we include its image (Figure 5-6), the monopole equates to a dipole for analysis. The fields vanish below the ground plane and restricting the fields to the upper hemisphere doubles the gain over a dipole, since only half the input power of the dipole is needed to produce the same field strength.

The input impedance decreases to half that of the equivalent dipole. We can form the image of the voltage source feeding the monopole in the ground plane. The voltage across the input of the equivalent dipole is twice that of the monopole to produce the same current. Therefore, the impedance of the monopole is half the impedance of the dipole.

The large value of edge diffraction greatly limits the F/B ratio of a monopole when it is placed on a finite ground plane. Figure 5-23 shows the pattern of a monopole when placed on 1λ-, 2λ-, and 10λ-diameter circular ground planes. The back radiation can be reduced by placing the monopole over a ground plane with circular corrugations that forms a soft surface at the edge when the corrugations are slightly deeper than $\lambda/4$ [10]. When the corrugations are less than $\lambda/4$, the ground plane can support surface waves.

5-10   SLEEVE ANTENNA [8, p. 422; 11, Chap. 5; 12; 13, p. 278]

A sleeve around the monopole (Figure 5-24) moves the virtual antenna feed up the monopole. The bandwidth increases because the current at the feed point remains nearly
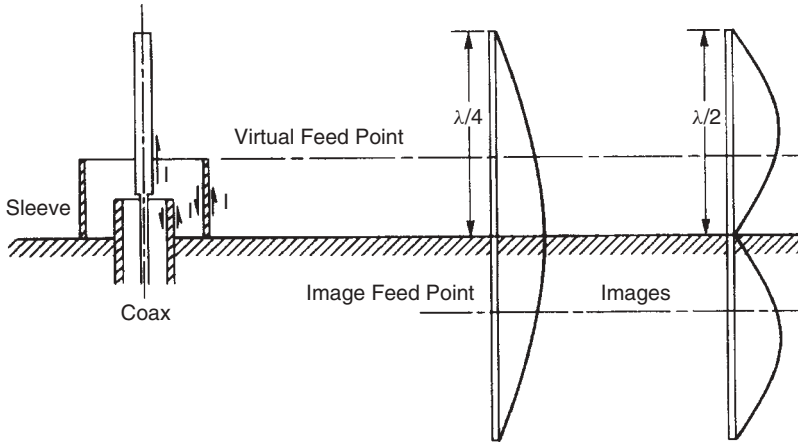
FIGURE 5-24   Sleeve monopole and current distributions.

constant over a wide band. Currents at the input for the case when the monopole is a quarter-wavelength long and when it is a half-wavelength long are about the same (Figure 5-24). The input resistance remains constant as the frequency changes.

The sleeve shields possible radiation from the internal currents while the currents on the outside of the sleeve radiate. The pattern changes little from that of an unshielded monopole. The internal structure is available as a series-matching stub and a trans-former to broadband the antenna. Design consists of adjusting the parts until a suitable compromise input impedance match is achieved over the band.

Dipole sleeve antennas (Figure 5-25) require symmetrical sleeves on the arms to maintain the symmetry of the currents. It is equivalent to feeding the antenna in two places. The balun is made an integral part of the base. In both antennas, strips or rods can replace the total coaxial sleeve [14]. The currents on the rods cancel the radiation from the currents on the internal feeder. Figure 5-26 illustrates an open-sleeve dipole using two rods designed to be mounted over a ground plane. The antenna is fed from a folded balun that consists of a grounded vertical coax with one pole connected to the outer shield and a matching tube connected to the second pole. The center conductor jumps across the gap to the second pole. Following are the design dimensions in wavelengths normalized to the lower-frequency band edge:

Dipole length	0.385	Dipole diameter	0.0214
Sleeve length	0.2164	Sleeve diameter	0.0214
Dipole-to-sleeve spacing	0.0381	Dipole height above ground	0.1644
Input taper	0.056		

Figure 5-27 plots the return-loss response of the antenna for various configurations and models of the antenna. The dipole without the sleeves has its best return loss over a narrow band centered at a normalized frequency of 1.05. The sleeves have little effect on this response at the low-frequency end. Adding sleeves produces a second resonance, which combines with the lower one to produce a broad bandwidth. An initial method of moments analysis used constant-diameter rods for the antenna, and Figure 5-27 shows the poor impedance match response of the antenna. A key element of the experimental
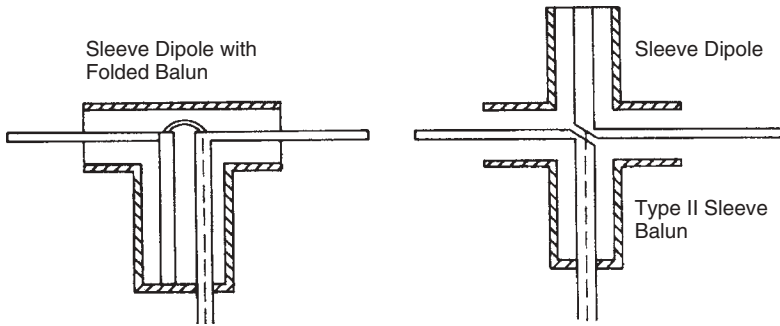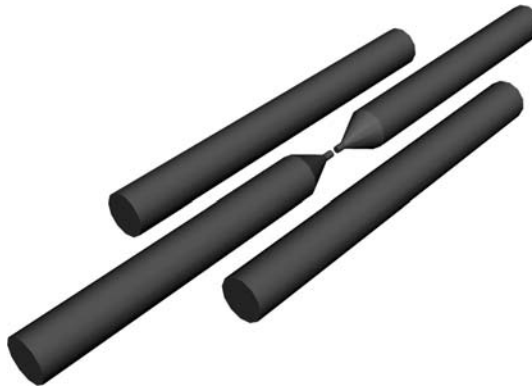
FIGURE 5-25   Sleeve dipoles.

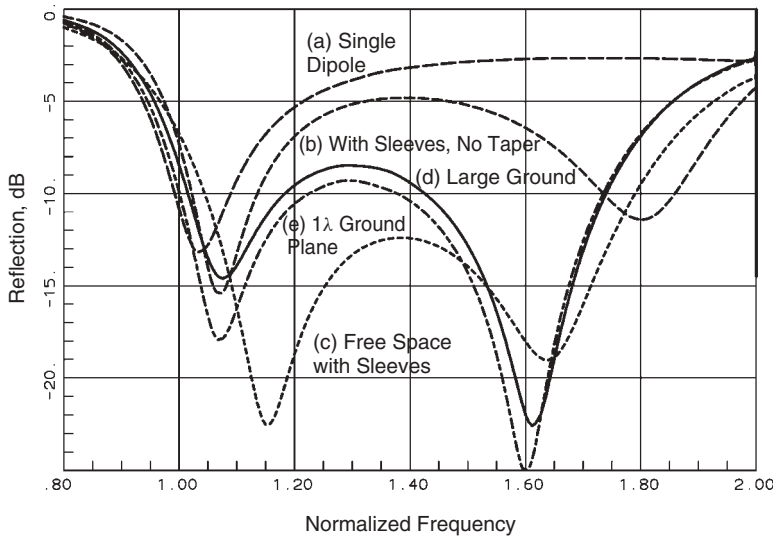**FIGURE 5-26**   Open-sleeve dipole with conical input taper.

FIGURE 5-27   Return-loss response of an open sleeve dipole: (*a*) dipole without sleeves; (*b*) open sleeve antenna; (*c*) open sleeve antenna with tapered input; (*d*) open sleeve antenna with tapered input located λ/4 over ground plane; (*e*) open sleeve antenna over a 1λ-diameter ground plane.

antenna is the tapered input. Adding this feature to the model produced the improved broad response of the experimental antenna. The constant-diameter model response shows a notable capacitive term on a Smith chart, and the tapered input produced the necessary inductance to reduce this effect. If the antenna is located in free space, the impedance response improves as shown. Figure 5-27 points out the importance of analyzing an antenna in its operating environment. The dot-dashed curve illustrates the response when the antenna was mounted over a one-wavelength-square ground plane. The finite ground plane produces a small but noticeable change in the input impedance. The effects of small changes in the analytical model warn us that we cannot expect antennas to match their models exactly and that small mechanical details can be used to improve performance.

An open-sleeve antenna can be made using a wire cage. Since the diameters of the dipole and sleeve rods are large, the weight can be reduced by using a circular array of wires for each conductor. The effective diameter of the cage, d_{eff}, is given as

$$d_{\text{eff}} = d \left(\frac{n d_0}{d} \right)^{1/n} \quad \text{or} \quad \frac{d_0}{d} = \frac{1}{n} \left(\frac{d_{\text{eff}}}{d} \right)^n \qquad (5\text{-}16)$$

The diameter of the individual wires is d_0, the cage diameter is d, and n is the number of wires.

5-11   CAVITY-MOUNTED DIPOLE ANTENNA

A dipole can be placed in a cup, and the assembly can be flush-mounted in a ground plane. The antenna shown in Figure 5-28 has disk sleeves located above and below the dipoles to stretch the bandwidth over a $1.8 : 1$ range [15]. Following are the dimensions normalized to the dipole length:

$$\frac{D}{L} = 2.57 \qquad \frac{H}{L} = 0.070$$
$$\frac{T}{L} = 0.68 \qquad \frac{G}{L} = 0.40 \qquad \frac{S}{L} = 0.505$$

The operating range is $0.416\lambda \leq L \leq 0.74\lambda$. The antenna cavity ranged from 0.28λ to 0.50λ deep and can no longer be considered thin. The cup antenna has a nearly constant gain (± 0.5 dB) of 10.5 dB over the band. Mounting the antenna in a cavity opens up new possibilities, because extra parameters are added to the design. At the low-frequency end, the cavity diameter is 1.07λ, which grows to 1.90λ at the high end.

We can use a dipole in a cup as a reflector feed. Excellent pattern and impedance response is obtained with the dipole mounted in a truncated cone cup with a 0.88λ aperture diameter, a 0.57λ-diameter base, and a 0.44λ depth [16, pp. 106–108]. The dipole is foreshortened to 0.418λ for an element diameter of 0.013λ and mounted 0.217λ above the base to achieve a 21% $2 : 1$ VSWR bandwidth for a single element. When we use a cross-polarized pair fed from a hybrid coupler to radiate CP, the impedance match at the input port improves. The signals reflected from the two dipoles add in phase at the isolated port and cancel at the input port. The load dissipates the reflected power, and the antenna through the hybrid presents an excellent impedance match.
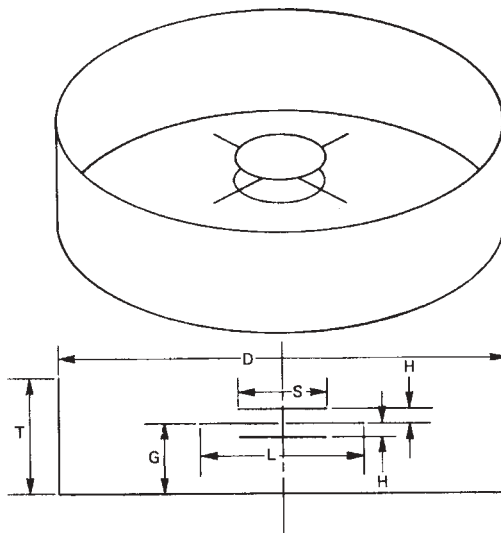
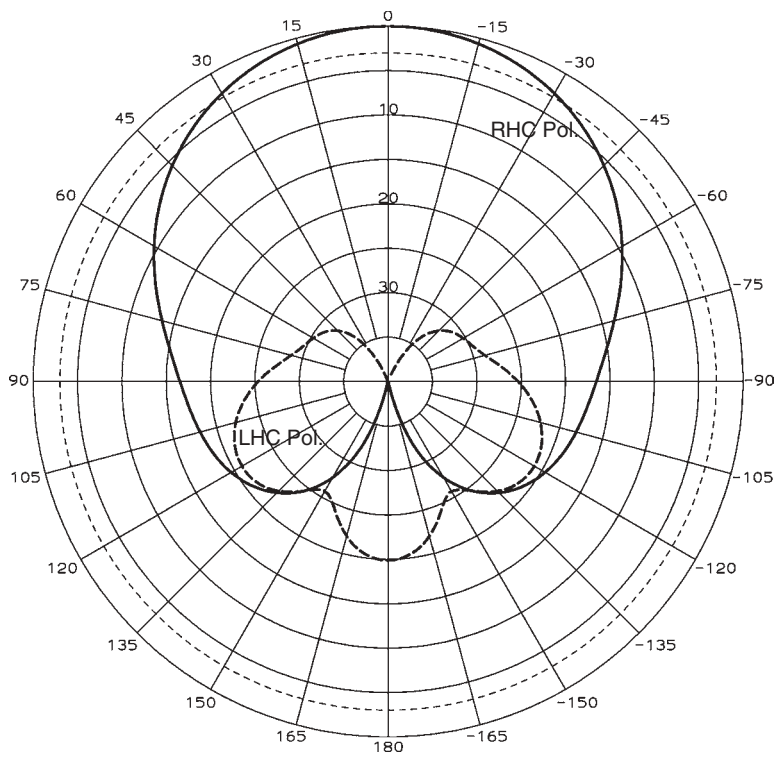**FIGURE 5-28**   Cavity-mounted sleeve dipole antenna.

FIGURE 5-29   Circular polarization response of a crossed dipole mounted 0.217λ above the bottom of a truncated cone 0.44λ deep with a 0.88λ aperture and a 0.57λ base.

TABLE 5-8   Illumination Losses When Pattern of Figure 5-29 Feeds a Paraboloidal Reflector

	Loss (dB)	
f/D	Average	Maximum
0.36	1.69	1.74
0.38	1.60	1.66
0.40	1.54	1.65
0.42	1.50	1.65
0.44	1.49	1.68
0.46	1.50	1.72
0.48	1.52	1.77
0.50	1.55	1.83
0.52	1.60	1.91

Figure 5-29 plots its pattern when excited for CP. The cross-polarization is about 30 dB below the peak co-polarization response over the entire 10-dB beamwidth cone. It has the following illumination losses when the antenna is used as a paraboloidal reflector feed (see Section 8-2); for $f/D = 0.44$ and averaged over the 21% bandwidth:

$$\text{spillover loss} = 0.72\,\text{dB} \qquad \text{amplitude taper loss} = 0.65\,\text{dB}$$

$$\text{cross-polarization loss} = 0.12\,\text{dB}$$

Table 5-8 demonstrates the broad optimum reflector f/D for a phase center 0.02λ inside the aperture plane, where we position it at the reflector focus.

5-12   FOLDED DIPOLE

A half-wavelength folded dipole increases the input impedance of a normal dipole fourfold while radiating the pattern of a single dipole. With the two elements closely coupled, we analyze the antenna using even and odd modes (Figure 5-30). The even mode divides the antenna into separate dipoles because the magnetic wall halfway between them is a virtual open circuit. The input current to the even mode becomes

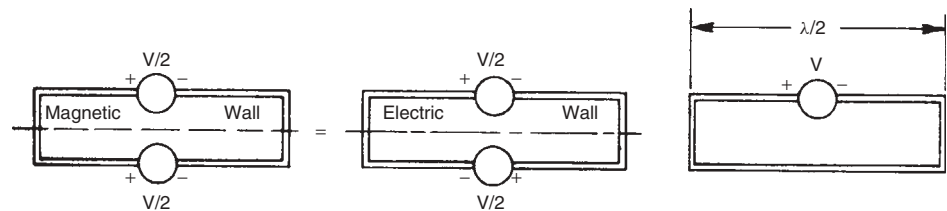$$I_e = \frac{V}{2(Z_{11} + Z_{12})}$$

FIGURE 5-30   Folded dipole analysis modes.

where Z_{11} is the self-impedance of one of the dipoles and Z_{12} is the mutual impedance between the closely coupled dipoles. The odd mode reduces the antenna to the series connection of two nonradiating $\lambda/4$ stubs:

$$I_o = \frac{V}{j Z_0 \tan(kL/2)}$$

where Z_0 is the characteristic impedance between the two rods. The input current is the sum of the even- and odd-mode currents. Near $L = \lambda/2$, the odd-mode current is quite small because its input impedance is an open circuit, and the input impedance is then determined by the even mode only:

$$Z_{\text{in}} = \frac{V}{I_e} = 2(Z_{11} + Z_{12})$$

For closely coupled lines, $Z_{11} = Z_{12}$ and the input impedance becomes $Z_{\text{in}} = 4Z_{11}$, where Z_{11} is the self-impedance of the dipole. Higher input impedance levels can be obtained by adding more elements.

A second method of altering the step ratio from 4 is to use unequal feed and shorted element diameters [17,18]. Given a driven element radius a_1, parasitic element radius a_2, and center-to-center spacing b, Hansen [18] gives a convenient formula for the step-up ratio $(1 + \gamma^2)$:

$$\gamma = \frac{\cosh^{-1}[(v^2 - u^2 + 1)/2v]}{\cosh^{-1}[(v^2 + u^2 - 1)/2uv]} \qquad \text{where} \quad u = a_2/a_1 \text{ and } v = b/a_1 \qquad (5\text{-}17)$$

5-13 SHUNT FEEDING [19, p. 118]

Shunt feeding grows out of the folded dipole. The T-match (Figure 5-31) starts as a folded dipole when the taps are at the ends. As the taps move toward the center, the impedance of the dipole dominates at first, since the admittance of the shunt stub in the odd mode is small and the input impedance is capacitive. At some point, as the taps move toward the center, the inductive admittance of the stub will cancel the capacitive admittance of the dipole and produce antiresonance with its high input resistance. The location and magnitude of this peak resistance depends on the diameters of the rods in the T-match section and the diameter of the radiator. The input resistance decreases as we continue to move the tap point toward the center after the feed location passes the antiresonance point. The input impedance is inductive and match is achieved by using symmetrical series capacitors. The T-match is fed from a balanced line.

The center short on the dipole allows the direct connection of the dipole to ground. Direct connection of broadcast towers (monopoles) to ground gives some lightning protection because the transmitter is capacitively connected to the tower. Shunt feeding with a T-match enables solid conductors, such as the skin of an aircraft, to be excited as a dipole. Horizontal shunt-fed dipoles can be connected directly to vertical towers with a metal-to-metal connection to increase the strength of the antenna to withstand adverse weather conditions.

A gamma match (Figure 5-31) can be fed from an unbalanced coax line. The shield of the coax connects to the shorted center of the dipole while the center conductor
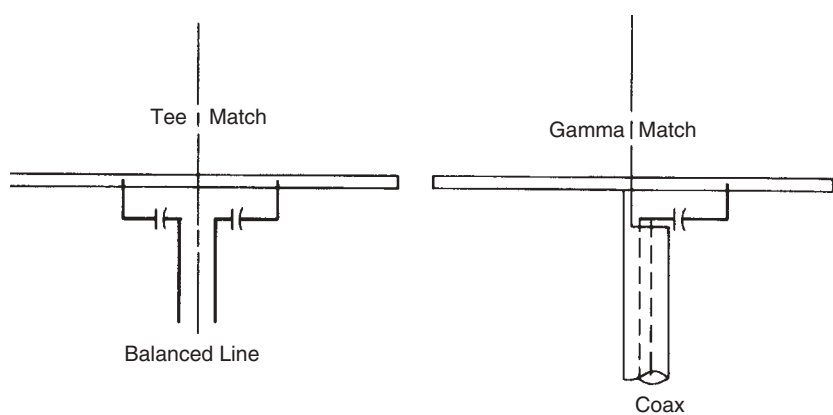
FIGURE 5-31   Shunt-fed dipoles.

taps into one side of the solid rod. Moving the tap away from the center increases the input resistance. The inductive reactance is series-tuned with a capacitor. Both of these connections reduce the bandwidth of the antenna as the input impedance is raised because the combination of the series capacitor and the shunt inductive stub increases the stored energy and Q of the antenna.

5-14   DISCONE ANTENNA

The discone antenna (Figure 5-32) is a modification of the dipole where the upper pole becomes a disk and the lower pole turns into a cone. We feed the antenna by locating a coax in the center of the cone and by connecting its outer shield to the lower cone at its top while we extend the coax center conductor and connect it to the disk. We obtain an antenna with a wide impedance bandwidth and a dipolelike pattern. As frequency increases the pattern peak moves toward the cone and gives a downward-pointing pattern. Figure 5-33 shows the pattern of a discone antenna at the design frequency and at two, three, and four times this frequency. The antenna produces less useful patterns as frequency increases. The antenna that gives the patterns in Figure 5-33 has a VSWR less than 3 : 1 from 1 to 10 times the design frequency. The cone upper diameter determines the high-frequency end of good impedance match. Typical slant length dimensions versus cone angle are as follows [20, pp. 128–130]:

Total Cone Angle	25	35	60	70	90
Slant Length (λ)	0.318	0.290	0.285	0.305	0.335

The upper disk diameter equals 0.7 times the lower cone diameter. The spacing between the top of the cone and the upper disk equals 0.3 times the diameter of the upper cone. The diameter of the upper cone determines the upper frequency limit, but practice shows that the antenna patterns are good only over a 4 : 1 to 4.5 : 1 frequency range. The impedance bandwidth is much wider than the pattern bandwidth. To reduce weight and wind loading, the cone and disk can be made from rods, with a typical implementation having at least eight.

FIGURE 5-32   Discone antenna with coaxial feed with a center conductor connected to the upper disk and a shield connected to the lower cone.
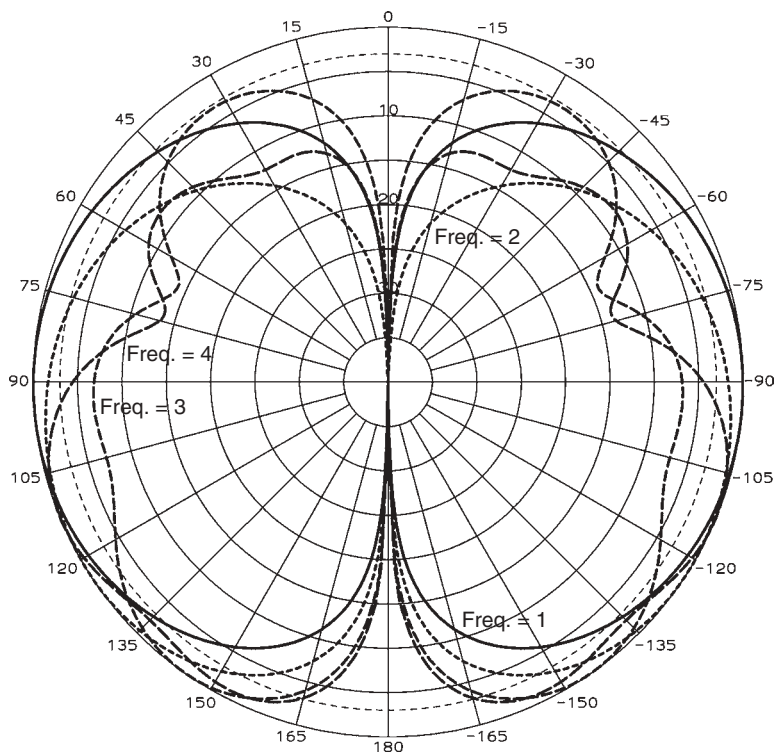

FIGURE 5-33   Elevation pattern of a $60°$ discone antenna at normalized frequencies $= 1, 2, 3,$ and 4.

5-15 BALUNS [21; 22, pp. 167–180]

A balun properly connects a balanced transmission line to an unbalanced transmission line. Simple arguments about impedances to the balanced and unbalanced modes of the three-wire transmission lines explain its operation. Considering one of the lines of a transmission line as ground misleads us. A ground plane under the transmission-line feeder becomes the third conductor of a three-wire line. Currents flowing in the ground plane can unbalance the currents in the feeder. A balanced three-wire transmission-line mode carries equal and opposite currents in the feeder lines. The capacitances per unit length of the two lines to ground are the same. Coax is an example of an unbalanced line structure (Figure 5-34). The inner conductor has no direct capacitance to ground. The two-wire line shown in Figure 5-34 is a balanced line having equal capacitances to ground, but we must judge a balanced line by the currents, not just the physical structure.

Before we analyze baluns, we must consider the fundamental modes of a three-wire transmission line. Figure 5-35 shows circuit representations of the modes without showing the ground conductor. Equal loads terminate ports 3 and 4. The even mode applies equal voltages on ports 1 and 2 and forms a magnetic wall between the conductors where the magnetic field vanishes to produce a virtual open circuit. The unbalanced mode—equal current directions—is associated with the even mode. Equal and opposite voltages on ports 1 and 2 form the odd mode and set up an electric wall between the conductors. The electric wall is a virtual short circuit. The odd mode excites equal and opposite currents—balanced mode—on the two lines. When the loads on ports 3 and 4 are unequal, the modes separate according to the voltages, even and odd, or the currents, unbalanced and balanced. Dipoles present loads between the lines and not to ground.
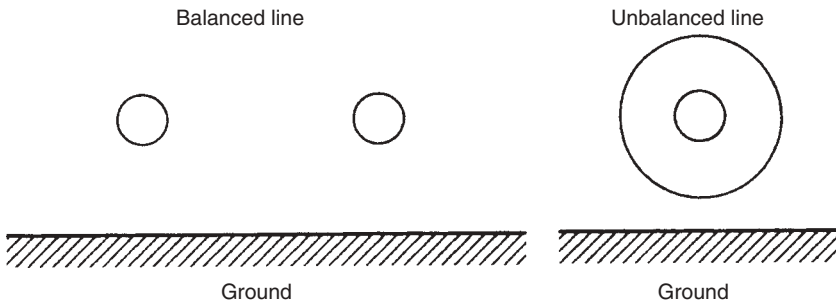

FIGURE 5-34 Physically balanced and unbalanced transmission lines.
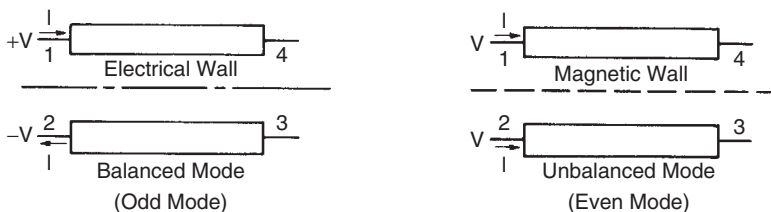

FIGURE 5-35 Balanced and unbalanced modes on a three-wire transmission line.

Unbalanced mode circuits radiate. Only closely spaced equal and opposite currents, the balanced mode, cancel the far-field radiation from the currents on the feed lines. The radiating feeder line adds radiation components to the antenna. These components can radiate unwanted polarizations and redirect the beam peak of the antenna (squint). In reception, the unwanted currents excited on the feeder by passing electromagnetic waves reach the receiver terminals without a balun to block them. We analyze baluns by using either transmitting or receiving antennas, depending on convenience, because reciprocity applies to baluns as well as antennas.

We detect balance problems from pattern squint and cross polarization. An impedance-measuring setup can detect some balance problems. Radiating unbalanced currents cause changes in the impedance. The radiation shows when the impedance changes as fingers are run over the coax line from the equipment. If we feed a dipole from a coax without a balun, the current on the outer conductor splits between the dipole conductor and the outside of the conductor. Patterns and impedance measurements detect this current. Unbalanced currents on the arms of the dipole and feeder currents cause pattern squint, but the cross-polarization radiated is usually a greater concern.

5-15.1 Folded Balun

A folded balun (Figure 5-36) allows the direct connection of a coax line to the dipole. A dummy coax outer conductor is connected to the pole fed from the center conductor. It runs alongside the feeder coax for $\lambda/4$ and connects to ground. The other pole connects directly to the shield of the feeder coax. The outer conductor of the coax and the extra line are two lines in a three-wire line with ground. We analyze the structure by using balanced (odd) and unbalanced (even) modes. Unbalanced-mode excitation
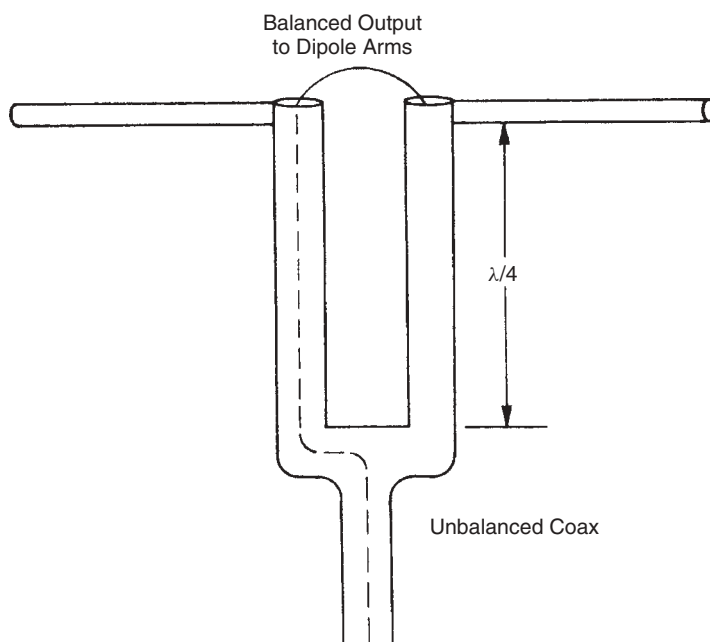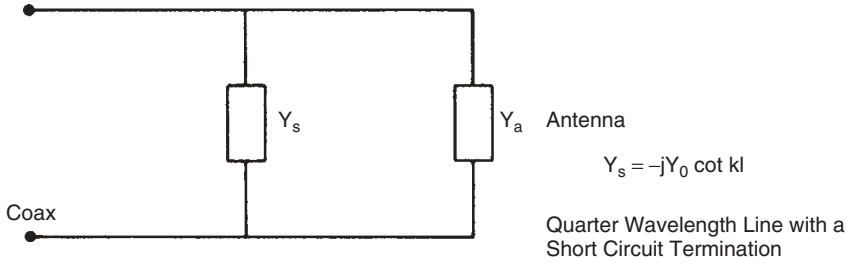

FIGURE 5-36 Folded balun.

**FIGURE 5-37** Folded balun equivalent circuit (balanced mode).

at the dipole forms a magnetic wall through the ground connection between the two coax shields. The circuit reduces to a single line with an open circuit at the ground connection. The open circuit transforms through the quarter-wavelength line to a short circuit at the dipole. Any unbalanced currents induced on the dipole or the coax outer conductor are shorted at the input. Balanced-mode excitation at the dipole forms an electric wall through the ground connection. The balanced-mode circuit of the two coax shields is a λ/4 short-circuited stub connected in shunt with the dipole (Figure 5-37). We analyze the frequency response from Figure 5-37. The bandwidth of the balun, although narrow, exceeds the bandwidth of the dipole. The Roberts balun [23] design adds an open-circuited stub λ/4 long inside the dummy coax of the folded balun. Instead of connecting the center conductor of feeding coax to the outer shield, we connect it to the open-circuited stub. The equivalent circuit for the balanced mode includes the short-circuited stub of the folded balun plus the open-circuited stub. The two reactances shift in opposite directions as frequency changes and produce a dual resonance we see as a loop on the Smith chart plot of impedance. The frequency bandwidth increases to almost $3 : 1$, a more suitable choice for wide-bandwidth antennas.

5-15.2 Sleeve or Bazooka Baluns

An outer jacket shields the outer conductor of the coax feeder in a sleeve balun (Figure 5-38). The sleeve and outer conductor of the coax form a series stub between the coax feeder and ground when the cup is short circuited to the coax outer conductor. The λ/4 stub presents a high impedance to the unbalanced currents at the top of the cup (Figure 5-39). A second sleeve below the first one and directed away from the dipole further prevents currents excited on the coax from reaching the input. When the frequency shifts, the connection to ground through the sleeve unbalances the transmission line. This balun is inherently narrowband.

Adding a stub to the center conductor (Figure 5-40) increases the bandwidth because the stubs track each other when the frequency changes. Figure 5-39 demonstrates the circuit diagrams of the two types of sleeve baluns. The type II sleeve balun has matching series stubs on the outputs. The lines remain balanced at all frequencies, but the stubs limit the bandwidth of efficient operation. Marchand [21] adds an open-circuited λ/4 stub inside the matching type II extra shorted stub of the sleeve balun and connects it to the coax center conductor in the same manner as the Roberts balun. The Roberts balun is a folded balun version of the Marchand compensated sleeve balun.

The coaxial dipole is a variation of the sleeve or bazooka balun. We rotate the right pole in Figure 5-38 until it is vertical and remove the left pole. We turn over the
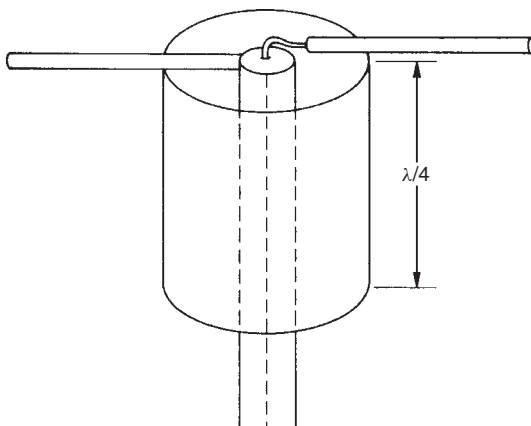
FIGURE 5-38   Sleeve or bazooka balun.
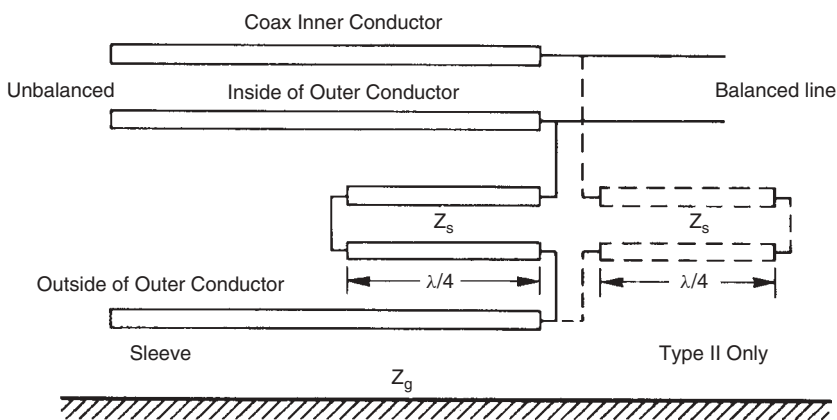
FIGURE 5-39   Schematic of types I and II sleeve or bazooka baluns.
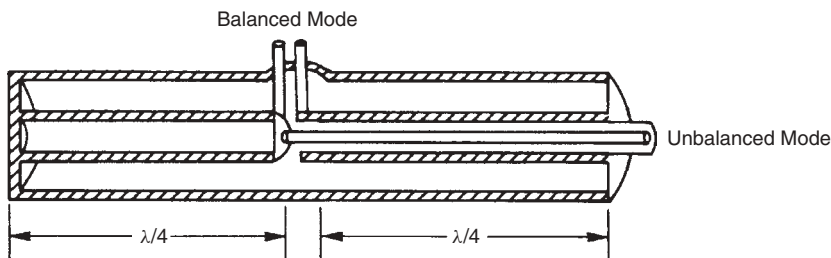
FIGURE 5-40   Type II sleeve balun.

sleeve and connect the short-circuit end to the outer conductor of the coax. The sleeve becomes the second pole of the dipole. The short-circuited stub at the bottom of the dipole between the outer conductor of the coax and sleeve transforms to an open-circuit impedance at the end of the lower pole. This prevents current flow farther down the coax. Some references call this a sleeve dipole, which should not be confused with the

sleeve dipole used to increase the impedance bandwidth. The coaxial dipole has the inherently narrow bandwidth of the bazooka balun, but is a convenient construction.

5-15.3   Split Coax Balun [24, p. 245]

A split coax balun allows the connection of both arms of a dipole to the outer shield of the coax that maintains symmetry to the dipole arms. Its rigidity helps to overcome vibration problems. Slots cut in the outer shield (Figure 5-41) enable the coax line to support two modes and make it equivalent to a three-wire line. A shorting pin excites the TE_{11} mode in the slotted coax (Figure 5-42) to feed the dipole in the balanced mode.

Analysis of a split coax balun is similar to that of a folded balun. The ends of the slots are equivalent to the ground connection of the two coax shields of the folded balun. A virtual open circuit forms at the ends of the slots in the unbalanced (even) mode. It transforms to a short circuit at the dipole and shorts the unbalanced mode at the input. The virtual short circuit at the end of the slots in the balanced mode transforms to an open circuit at the input. Figure 5-37 gives its circuit diagram.

Symmetry improves the performance of a split coax balun over a folded balun. The shorting pin is used only to excite the TE_{11} mode to feed the dipole arms. The extra wire length of the center conductor jumper of the folded balun introduces phase shift to the second arm and squints the beam. For that reason, the split coax balun is a better high-frequency balun. The phase shift problem of the jumper also occurs with the "infinite" balun of the log-periodic antenna.
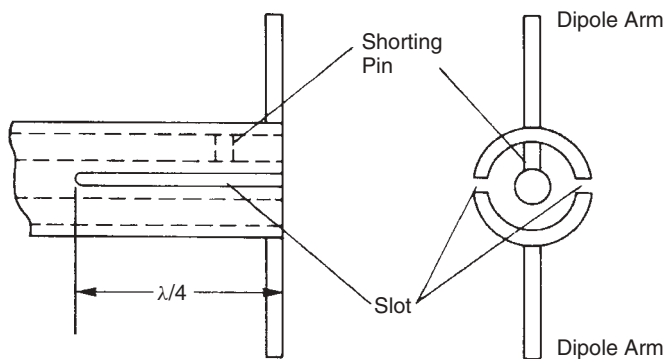

FIGURE 5-41   Split coax balun. (From [24], Fig. 8-5, © 1948 McGraw-Hill.)
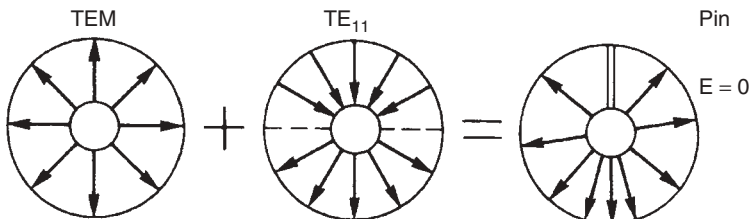

FIGURE 5-42   Coaxial transmission-line modes in a split coax balun. (From [24], Fig. 8-6, © 1948 McGraw-Hill.)

5-15.4   Half-Wavelength Balun

A half-wavelength balun (Figure 5-43) works by cancellation of the unbalanced-mode currents at the input to the coax. The impedance transforms by a factor of 4 from unbalanced- to balanced-mode ports. In the unbalanced (even) mode, equal voltages are applied to the two output ports. When the voltage wave on the upper line propagates through $\lambda/2$, its phase changes by $180°$. This signal cancels the signal connected directly to the coax center conductor.

A load across a balanced-mode transmission line has a virtual short circuit halfway through it. The load on each balanced-mode line is $2Z_0$, where Z_0 is the coax characteristic impedance. The load on the end of the $\lambda/2$-long line is transformed by the transmission line to the identical impedance when it circles the entire Smith chart. The two loads, each $2Z_0$, are connected in shunt at the coax input and combine to Z_0. A balanced-mode impedance of $4Z_0$ transforms to Z_0 at the coax input. The $\lambda/2$-long cable can be rolled up for low frequencies. The balun transforms 300-Ω input impedances of folded dipoles to 75 Ω by using RG-59 cable (75 Ω).

5-15.5   Candelabra Balun

A candelabra balun (Figure 5-44) transforms the unbalanced-mode impedance fourfold to the balanced-mode port. The coax cables on the balanced-mode side connect in series, whereas those on the unbalanced-mode side connect in parallel. We can divide the balanced-mode impedance in two and connect each half to a $2Z_0$ impedance transmission line. These lines then connect in shunt at the unbalanced-mode port. The unbalanced-mode currents short out at the input to the $2Z_0$ coax lines in the same manner as does the folded balun. More lines can be stacked in series and higher-impedance transformations obtained, but construction becomes more difficult.

5-15.6   Ferrite Core Baluns

Ferrite cores can be used to increase the load impedance to unbalanced-mode currents and reduce them. At low frequencies (<100 MHz) ferrite has high permeability. As the frequency increases, the permeability drops, but the losses to internal magnetic fields increase. The increased inductance of transmission lines is used at low frequencies, and the increased loss is used at high frequencies to inhibit currents.

Ferrite bazooka or sleeve balun ferrite cores, placed on the outside of a coax line (Figure 5-45), increase the impedance to ground for currents on the outside of the
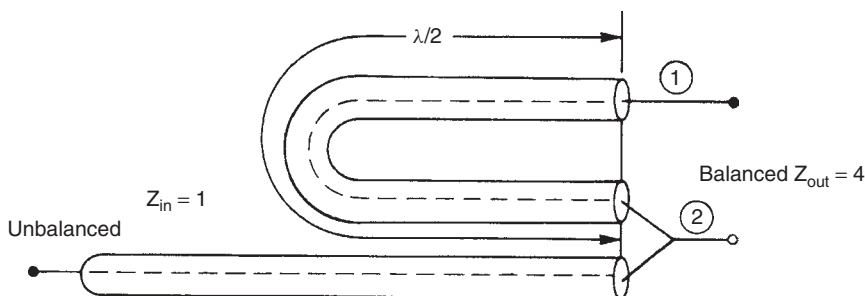

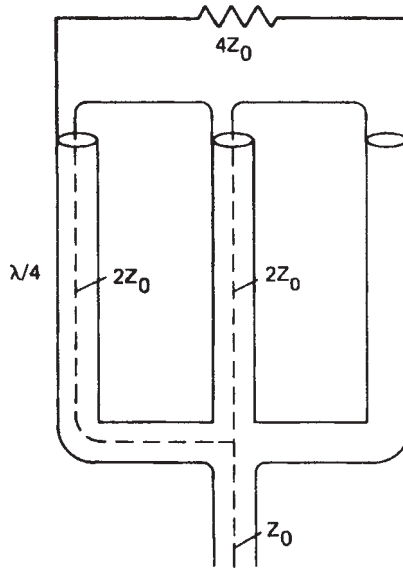**FIGURE 5-43**   Half-wavelength balun.
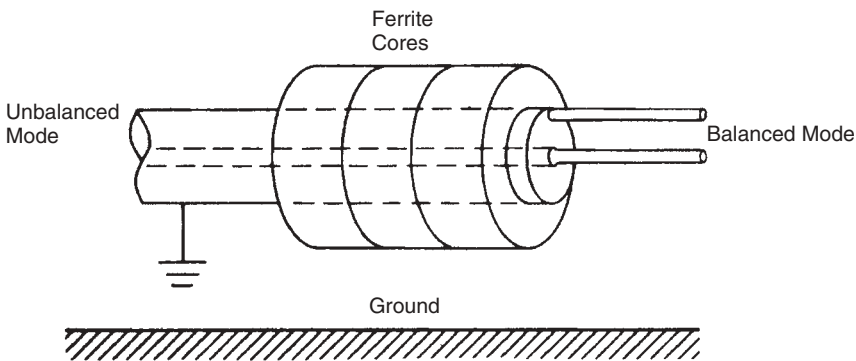
FIGURE 5-44   Candelabra balun.

FIGURE 5-45   Ferrite core bazooka balun.

shield and inhibit unbalanced currents between the ground and the outer shield. The ferrite balun can work over many decades. The ferrite material provides high impedance through inductance at low frequencies. As the ferrite material impedance drops when frequency increases, the transmission line approaches $\lambda/4$ of the bazooka balun. Any ferrite core balun is a compromise design between low-frequency response controlled by the amount of ferrite and high-frequency response controlled by the length of transmission line.

Bifilar wire windings on a ferrite core form the $1:1$ balun (Figure 5-46a). The bifilar wire closely approximates 50- to 100-Ω characteristic impedance transmission lines. This balun can work satisfactorily from 100 kHz to 1 GHz. When there are balanced currents in the windings, there is no net magnetic field in the ferrite. In the unbalanced mode, the fields add in the core and give a high series impedance due to the high inductance (low frequency) or high resistance (high frequency). The amplitude at port
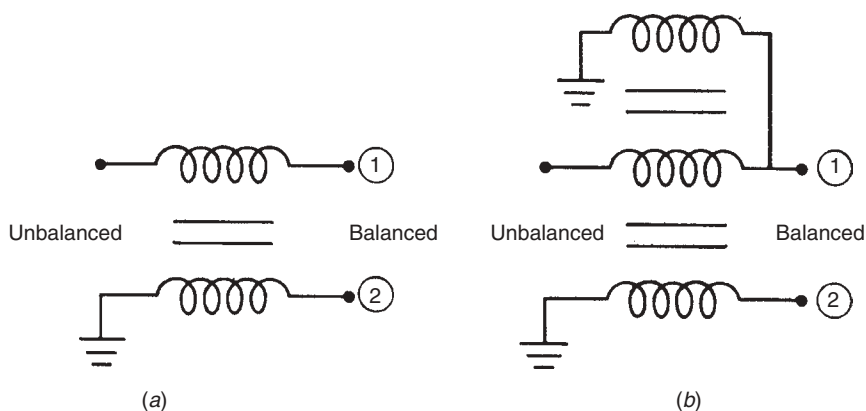
FIGURE 5-46   Bifilar wire ferrite core baluns: (*a*) type I; (*b*) type II.
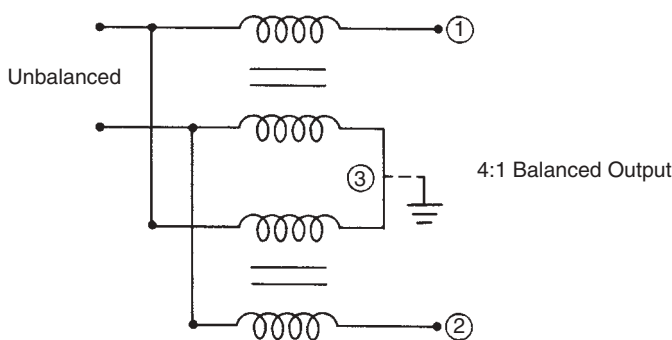
FIGURE 5-47   Ferrite core candelabra balun.

2 (Figure 5-46*a*) is lower than at port 1 because of the extra losses introduced in the ground lead by the ferrite core. This can be corrected by adding an extra winding to ground (Figure 5-46*b*), which produces a type II bazooka balun. The extra winding balances the outputs by adding loss to port 1 without any increase in bandwidth due to the ferrite loading.

5-15.7   Ferrite Candelabra Balun

We can make a parallel-to-series ferrite balun that transforms the unbalanced-mode input impedance fourfold to the balanced-mode output (Figure 5-47). As in the coax version, the characteristic impedance between the wires in the cores should be twice the unbalanced-mode input impedance. Point 3 (Figure 5-47) is a virtual short. Connecting it to ground sometimes helps the balance. Both windings can be wound on the same core, such as a binocular core.

5-15.8   Transformer Balun

A transformer balun has no transmission-line equivalent; it is merely a transformer (Figure 5-48). The balanced-mode output impedance is fourfold that of the input

FIGURE 5-48   Ferrite transformer balun.

unbalanced mode. Wound with trifilar wire, the output has twice the number of turns compared to the input, and each output line has the same impedance to ground th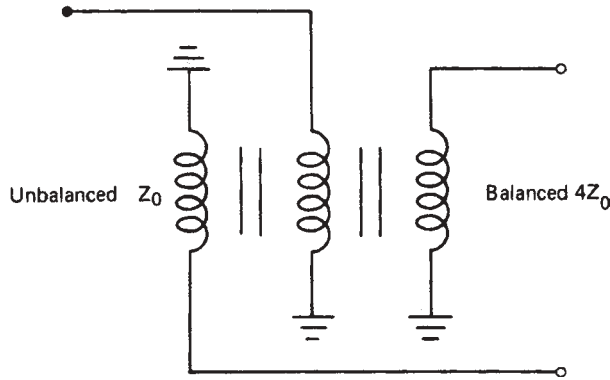rough the transformer. No transmission-line effects extend the upper band edge beyond the transformer action of the windings and ferrite, but the transformer balun is a fine low-frequency device. Use of No. 36 and 38 wires in ferrite core baluns limits the power-handling capability of the baluns to receive-only levels. The ferrite bazooka balun (Figure 5-45) carries the power in coax, which allows higher power levels.

5-15.9   Split Tapered Coax Balun [25]

A split tapered coax balun starts with inherently unbalanced coax. Moving toward the balanced end, an outer conductor slot opens and exposes more and more of the center conductor (Figure 5-49). At the point where the size of the outer conductor is reduced to that of the inner conductor, we connect a balanced twin line to the two conductors. The impedance must be raised from input to output, since the two-wire line, spaced the radius of the coax, has higher impedance than the one at the coax input. The balance depends on reducing the reflected wave in the transformer. Any suitable tapered transformer, such as Dolph–Chebyshev or exponential, can be used, and design return loss is the level of the unbalanced mode. The balun can be constructed in microstrip. The ground plane tapers until it and the upper conductor are the same size. This balun can operate over decades of bandwidth, since the tapered transformer determines the bandwidth.
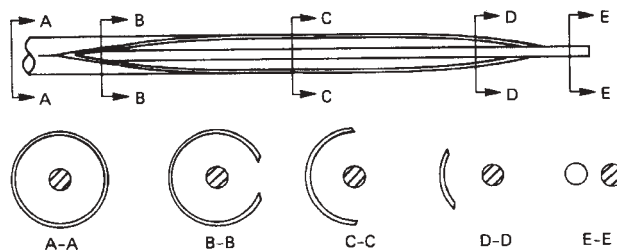

FIGURE 5-49   Split tapered coax balun. (From [16], Fig. 1, © 1960 IEEE.)

5-15.10 Natural Balun [26, p. 821]

A natural balun feeds the coax through a loop antenna to the feed point where the outer shield is split and the center conductor jumps the gap to connect to the outer shield of the coax. At this point the currents flow on to the outer shield and radiate. By moving an equal distance along the coax until the two halves meet, we can connect the feed coax and not have current flow down the outside. The currents flow in opposite directions along the loop and cancel at the connection. From a circuit point of view, the connection point is a virtual short circuit to the balanced mode similar to a folded balun at its connection point. In a similar manner, on a folded dipole we can connect the feed coax to the middle of the shorted dipole and form a natural balun.

We have not exhausted the number of balun designs. The "infinite" balun of log-periodic antennas will be discussed as part of the construction of such antennas. When a broad-beam antenna is designed, sometimes a little squint in the beam and a little cross-polarization are acceptable and the antenna may be fed without a balun.

5-16 SMALL LOOP

In Section 2-1.2 we discuss the radiation from a small constant-current loop. For a small loop the current is approximately constant and has the pattern of a short magnetic dipole located along the axis of the loop. Similar to the short dipole, we calculate the series resistance and radiation resistance to calculate efficiency. We increase efficiency by adding closely coupled turns and ferrite rods to increase the magnetic field. A multiturn loop with N turns and loaded with ferrite with an effective permeability μ_{eff} and area A has a radiation resistance:

$$R_{\text{loop}} = 320 N^2 \mu_{\text{eff}} \pi^4 \frac{A^2}{\lambda^4}$$

The wire adds a series loss resistance R_L to the input resistance of the multiturn loop, but it is proportional to N instead of N^2 and the wire surface resistance R_s given the wire conductivity σ:

$$R_L = \frac{(\text{loop length}) N R_s}{\text{perimeter of wire cross section}}$$

$$R_s = \sqrt{\frac{\omega \mu_0}{2\sigma}}$$

When we have a circular loop radius b and a wire diameter of $2a$, we find a series inductance from the loop:

$$L_{\text{loop}} = \mu_0 \mu_{\text{eff}} N^2 b \ln \frac{b}{a}$$

$$R_L = \frac{b}{a} R_s$$

The radiation efficiency of the loop is calculated by using the series-loss resistance and the radiation resistance:

$$\eta_e = \frac{P_r}{P_{\text{in}}} = \frac{R_{\text{loop}}}{R_{\text{loop}} + R_L}$$

Adding turns and ferrite material increases the radiation efficiency.

We compute the mean effective permeability by integrating along the ferrite rod the permeability distribution $\mu_c(x)$ of the core and dividing by its length [27, p. 6-20]. The following approximates its distribution for a core of length l:

$$\mu_c(x) = \mu_{cs}(1 + 0.106\overline{x} - 0.988\overline{x}^2)$$

$$\overline{x} = \frac{2|x|}{l}$$

The factor μ_{cs} depends on the ferrite geometry. For a cylindrical rod with diameter D, we calculate μ_{cs} from

$$\mu_{cs} = \frac{\mu}{1 + (\mu - 1)(D/l)^2(\ln(l/D)\{0.5 + 0.7[1 - \exp(-\mu \times 10^{-3})]\} - 1)}$$

For a rectangular cross section of height h and width w ($w \geq h$), we find μ_{cs} from

$$\mu_{cs} = \frac{\mu}{1 + (\mu - 1)(4wh/\pi l^2)\{\ln [\beta l/(w + h)] - 1\}}$$

$$\beta = 4 - 0.732\left[1 - \exp\left(-5.5\frac{w}{h}\right)\right] - 1.23\exp(-\mu \times 10^{-3})$$

When the axis of the loop is along the z-axis, the effective height **h** is determined by the area:

$$\mathbf{h} = -j\overline{\mu}_{\text{eff}}kA\sin\theta\hat{\boldsymbol{\theta}}$$

The ferrite loop antenna finds use as a receiving antenna at low frequencies where the sky noise is very high, and the added noise of the antenna due to poor efficiency has little effect on the overall G/T value.

5-17   ALFORD LOOP [28]

An Alford loop feeds two dipoles curved into a loop that radiates an omnidirectional pattern with horizontal polarization when located horizontally over a ground plane. Figure 5-50 shows a configuration fed from coax where it feeds two parallel-plate transmission lines connected in shunt. The flat dipoles and the sides of the transmission line are offset by a central substrate (not shown). The opposite direction of the dipoles produces a $180°$ phase shift between them. The odd-mode feed produces a pattern null along the coax axis that reduces current excitation on the outside of the coax and eliminates the need for a balun. We space the loops so that the circumference is approximately 1λ and adjust the parallel-plate line impedance to transform the dipole impedance to $100\,\Omega$ where the two sides are connected in shunt.

The horizontal pattern improves when we place the Alford loop in a slotted cylinder [29]. Figure 5-51 illustrates the positioning of the loop in the slotted cylinder when viewed from below before it is attached to a ground plane. The 0.38λ-diameter cylinder has four slots each 0.5λ long with open-circuited ends. We cut an opening about 0.2λ along the circumference about 0.12λ along the cylinder axis to create an open circuit for the slot where the cylinder attaches to the ground plane. Of course,
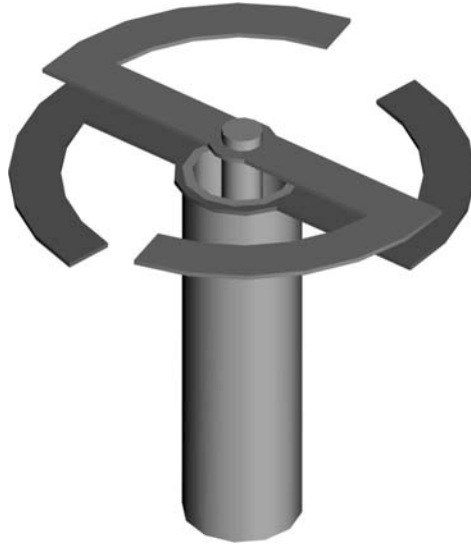
FIGURE 5-50 Alford loop fed by coax into a parallel-plate transmission line.
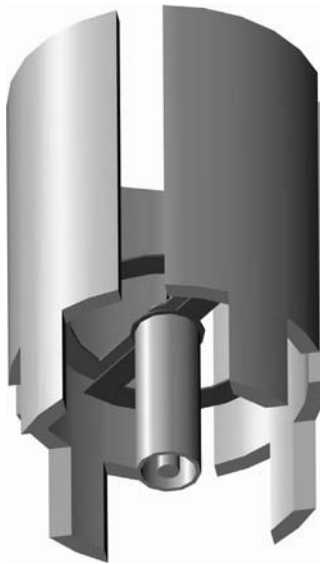
FIGURE 5-51 Alford loop feeding slotted cylinder viewed from below where connected to ground plane.

the coax runs through the ground plate to its connector. We point the parallel-plate transmission line halfway between two slots so that each curved dipole feeds two slots. Figure 5-52 gives the typical pattern of the antenna on a ground plane. This antenna illustrates another example of the interaction of dipoles and slots used to improve patterns.
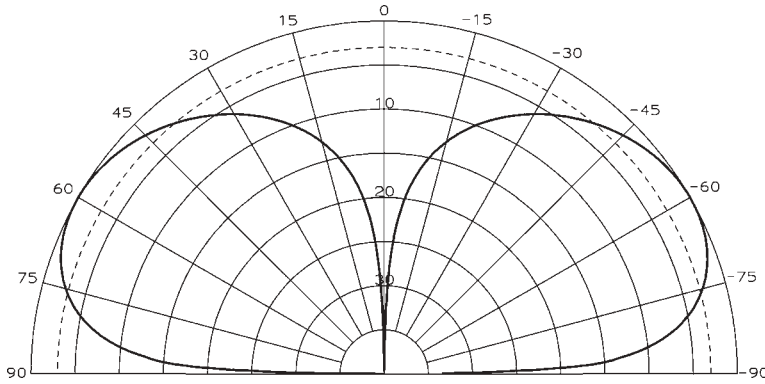
FIGURE 5-52   Horizontally polarized pattern of Alford loop feeding slotted cylinder.

5-18   RESONANT LOOP [19, p. 158; 30]

A folded dipole has a perimeter of one wavelength, and any other shaped loop will resonate when its perimeter is near one wavelength. The sinusoidal current distribution of the folded dipole remains on the loop. The folded dipole has a dipole pattern with its null in the direction of the voltage across the feed. The loop retains this pattern property when it is symmetrical about the feed point. The loop shape that opens in the *H*-plane distorts the normal perfect-circle *H*-plane pattern of the dipole and gives 3- to 4-dB peaks in the directions normal to the loop compared with the directions in the plane of the loop. The *E*-plane null is filled in with a cross-polarized pattern at about 20 dB below the beam peak.

Since the current distribution is sinusoidal on the loop, opposite the feed and halfway around the loop perimeter is a virtual short-circuit point. The current reaches maximums at the virtual short circuit and at the feed. We can expect a moderate input resistance because the standing-wave current is high. A circular loop has an input resistance of about 130 Ω when the loop is 1.08 wavelengths in perimeter. If the loop is a parallelogram, the resonant input resistance depends on the angle between the wires at the feed. The resistance starts at about 300 Ω for the folded dipole and decreases for decreasing angles. At 120° between the lines, the resistance is about 250 Ω and drops to 50 Ω when the angle is 60°. Four common loop shapes are: (1) circle, (2) square (quad), (3) parallelogram, and (4) triangle. Changes in the shape affect the input resistance at resonance and, to a slight degree, the resonant perimeter. The *Q* of the antenna is about the same as that of a half-wavelength dipole. The gain equals that of the one-wavelength dipole, 3.8 dB.

Figure 5-53 illustrates a resonant loop used as a ground plane for a dipole spaced at $\lambda/4$ above it. Each square is $\lambda/8$ on a side with a center square with mounting holes for the balun. The ground plane consists of two resonant loops, because the center ring is eight squares around, while the outer ring has 16 squares for a 2λ loop. For this antenna each pole consists of two rods: one horizontal and one tilted at 30°. Two versions of this antenna landed on Mars in 1976 [31]. Not only is the ground plane extremely lightweight, but it gives an excellent F/B ratio for a ground plane only 1λ across. We can easily add a resonant ring to an antenna—whether a dipole or another antenna—and expect an improvement.
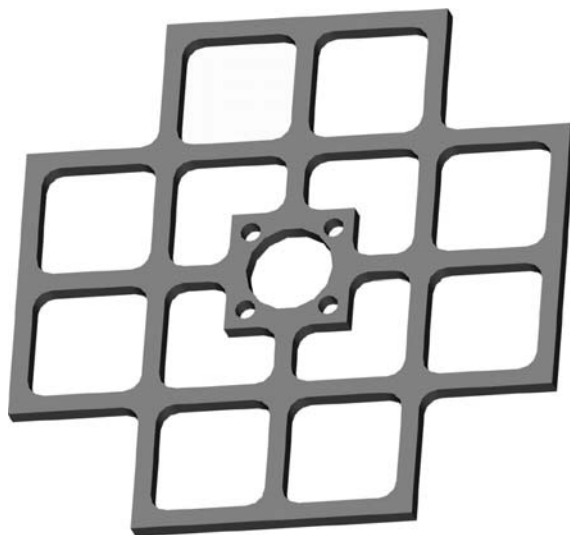
FIGURE 5-53 Combined 1λ and 2λ resonant loops ground plane for crossed dipoles using $\lambda/8$-side squares.

5-19 QUADRIFILAR HELIX [32, 33]

A quadrifilar helix consists of two interwound resonant loops twisted into a helical shape. Although the antenna can be made using two open U-shaped wires, the usual implementation has two loops. The loop quadrifilar helix is resonant when each loop has a perimeter slightly greater than one wavelength, similar to a planar resonant loop. The feed produces a standing-wave current distribution that peaks at the feed and at the center of the shorting wire that joins the two ends of the helix. Nulls in the current distribution occur halfway along the helical section. The lower half of the antenna can be removed at the null points to form a dual open U-shaped antenna. An antenna using a half-turn in each of the four arms of the helix with a diameter of 0.174λ and a height of 0.243λ produces a circularly polarized pattern with a $120°$ beamwidth when fed from two equal-amplitude feeds phased in quadrature.

If we consider a single twisted loop oriented with the z-axis along the helix axis, we discover the unique radiation characteristics by doing a MOM analysis of the wire loop. The analysis shows equal and opposite currents located on the feed and shorting line that reduces the radiation from the closely spaced straight sections. The currents along the helical section have a progressive traveling-wave phasing except for the $180°$ phase shift through the null. This traveling-wave current radiates circular polarization.

Consider a loop twisted into a right-hand helix. The loop radiates a pattern with lobes along the $+z$- and $-z$-axes, both with left-hand circular polarization. If we rotate the helix end to end, the helix remains right-hand and the problem has not changed. Whether we feed the antenna at the top or bottom in the center of the straight wire, the current distribution on the antenna is the same and the pattern has the same polarization. When we feed both loops with phasing for left-hand circular polarization (x-axis $0°$ and y-axis $90°$) on the right-hand helix, the two left-hand circularly polarized lobes from the two loops add along the z-axis, while the left-hand lobes along the $-z$-axis

cancel because the feeding phases are for RHC along the $-z$-axis. Of course, we use a left-hand helix and right-hand feeding phases for RHC polarization.

Figure 5-54 shows a left-hand half-turn quadrifilar helix that radiates RHC. Normal practice uses a dual folded balun to feed the antenna, with the two ports connected to a hybrid coupler to produce circular polarization. The balun short circuit is a disk located $\lambda/4$ from the feed through which all four coax cables pass. We solder the coax lines to the disk to complete the folded balun structure. We add two upper jumper wires at the feed points. We can use the balun structure to support the two helixes as shown in Figure 5-54. A second construction uses self-supporting helixes fed at the lower end by a dual balun. Out of band this antenna also suffers from poor efficiency even though the antenna is well matched at the hybrid port, because the equal reflections from the two loops are routed to the load on the hybrid coupler. Although mutual coupling between the two twisted loops modifies the input impedance, we discover that each individual loop has nearly the same impedance as the total antenna.

We can feed a quadrifilar helix from a turnstile feed if we use unequal perimeter twisted loops to produce a phase difference caused by the impedance changes when the loop is longer or shorter than a resonant length. A development similar to Section 5-6 gives us the dimensional changes of the loops required to produce a circularly polarized pattern. For a half-turn helix the perimeter length determines the resonant frequency:

$$\text{perimeter} = \sqrt{(2 \cdot \text{height})^2 + (\pi \cdot \text{diameter})^2} + 2 \cdot \text{diameter} \qquad (5\text{-}18)$$

By Section 5-6 the ratio of the two perimeters that will produce a circularly polarized pattern is related to antenna bandwidth (Q). If we keep the same diameter (D) for both helixes, we modify the heights (H):

$$\frac{\sqrt{(2H_1)^2 + (\pi D)^2} + 2D}{\sqrt{(2H_2)^2 + (\pi D)^2} + 2D} = 1 + \frac{1}{Q} \qquad (5\text{-}19)$$

FIGURE 5-54   Half-turn quadrifilar helix fed from two folded baluns.

This allows the feed to be a split-tube balun when the two loops are joined to the same coax balun located in the center. We split Eq. (5-19) in the same manner as Eq. (5-11) to compute the two new heights:

$$\sqrt{(2H_x)^2 + (\pi D)^2} + 2D = \frac{\sqrt{(2H_0)^2 + (\pi D)^2} + 2D}{\sqrt{1 + 1/Q}} \qquad \text{for RHC}$$

$$\sqrt{(2H_y)^2 + (\pi D)^2} + 2D = \left[\sqrt{(2H_0)^2 + (\pi D)^2} + 2D\right]\sqrt{1 + 1/Q}$$

(5-20)

A half-turn quadrifilar helix with diameter $= 0.174\lambda$ and height $= 0.243\lambda$ has a 3.2% $2:1$ VSWR bandwidth. We determine antenna Q by using Eq. (5-10) to be equal to 22.1. We use Eq. (5-18) to calculate the perimeter of the unmodified helix to be 1.079λ. When we substitute the Q and the perimeter into Eq. (5-20), we can easily solve for the two heights: $H_x = 0.2248\lambda$ and $H_y = 0.2608\lambda$. This assumes that the antenna has a left-hand helix for RHC polarization. When we make this antenna with the correct dimensions, the measured Smith chart of the design will have a small loop at the frequency with the least cross-polarization. The two shorted loops do not meet at the point opposite the feed but pass over and under each other. We can design a turnstile quadrifilar helix with the same height for the two loops by using Eq. (5-20) to compute the two diameters.

5-20   CAVITY-BACKED SLOTS

A slot that radiates only on one side of the ground plane is the dual of a monopole. As in the case of the monopole, restricting the radiation to above the ground plane doubles the gain. The voltage across the slot determines the field strength. Since the radiated power is only half that of the slot radiating on both sides and having the same peak fields, the input impedance doubles. The already high slot impedance becomes even higher. The cavity must present an open circuit at the slot, or its susceptance must combine with the slot susceptance to resonate. Normally, it is a quarter-wavelength deep. Since many cavities form a box, the waveguide mode determines the propagation constant (wavelength) used to determine the depth.

5-21   STRIPLINE SERIES SLOTS

Stripline consists of a center strip equally spaced between two flat ground planes. It supports a coaxial-type TEM-mode wave between the central strip and the two ground planes. The ground plane currents match the currents flowing in the central strip. A waveguide has axial currents that flow along the axis and transverse currents that flow in the direction of the sidewalls. Any slots cut in the ground plane can only interrupt axial currents and present series loads to the transmission line because the TEM wave has no transverse currents. The load that a slot presents to the transmission line is a parallel combination of a radiation conductance and an energy storage susceptance. Low values of inductive reactance shunt power around the high resistance of short slots. The inductance increases with increasing electrical length and supports higher voltages across the slot radiation resistance. This increases the radiated power. The

inductance increases to an antiresonance near $\lambda/2$, where further increases in electrical length decrease the capacitive reactance.

Oliner [34] gives an expression for slot conductance normalized to the stripline characteristic impedance. When unnormalized, it becomes

$$G = \frac{8\sqrt{\varepsilon_r}}{45\pi^2}\left(\frac{a'}{\lambda}\right)^2\left[1 - 0.374\left(\frac{a'}{\lambda}\right)^2 + 0.130\left(\frac{a'}{\lambda}\right)^4\right] \tag{5-21}$$

where a' is the length of the slot and ε_r is the dielectric constant of the stripline boards. More complete expressions for full series admittance are available [35], but near resonance Eq. (5-21) suffices.

Most striplines are etched on dielectric substrates. The dielectric fills the slot and reduces the resonant length. The effective dielectric constant in the slot is [36]

$$\varepsilon_r' = \frac{2\varepsilon_r}{1 + \varepsilon_r} \tag{5-22}$$

Slot length determines the radiation conductance. Decreasing the resonant length increases radiation resistance at resonance.

Example A set of woven Teflon fiberglass ($\varepsilon_r = 2.55$) dielectric boards supports a resonant-length slot in a stripline circuit. Compute resonant length and center-fed radiation conductance for a slot that resonates when $a' = 0.48\lambda$ in air.

The effective dielectric constant from Eq. (5-22) is 1.44. The effective dielectric constant reduces the resonant length:

$$\frac{a'}{\lambda} = \frac{0.48}{\sqrt{1.44}} = 0.40$$

Equation (5-21) finds the resonant conductance as $3.27\,\text{mS}$ or $306\,\Omega$ resistance. The high impedance requires an offset feed to match the slot to a stripline. We locate the offset feed from the slot center to reduce the input impedance:

$$\xi = \frac{a'}{2} - \frac{\lambda}{2\pi\sqrt{\varepsilon_r'}}\sin^{-1}\sqrt{\frac{Z_{\text{in}}}{Z_c}} \tag{5-23}$$

We can determine the 50- and 100-Ω feed points of the slot:

$$50\,\Omega:\quad \xi = \frac{0.40\lambda}{2} - \frac{\lambda}{2\pi\sqrt{1.44}}\sin^{-1}\sqrt{\frac{50}{306}} = 0.145\lambda$$

$$100\,\Omega:\quad \xi = \frac{0.40\lambda}{2} - \frac{\lambda}{2\pi\sqrt{1.44}}\sin^{-1}\sqrt{\frac{100}{306}} = 0.119\lambda$$

At $2\,\text{GHz}$, the dimensions of the slot and the feed locations become:

$$a' = 6\,\text{cm}:\quad \xi = 2.17\,\text{cm}\ (50\,\Omega) \qquad 0.83\,\text{cm from edge}$$

$$\xi = 1.79\,\text{cm}\ (100\,\Omega) \qquad 1.21\,\text{cm from edge}$$

Increasing the slot width decreases the impedance below that of the thin-width slot result given above and will require experimental work to find the exact feed point. Measuring the center-fed impedance allows the use of Eq. (5-23) to compute the approximate offset feed point.

Figure 5-55 illustrates a typical stripline-fed slot. Shorting the center strip to ground at the location of the slot creates a current maximum at the slot for feeding. An open circuit a quarter wavelength beyond the slot creates the same standing-wave current maximum at the slot. Convenience determines the feeding method. The slot interrupts currents only in the top ground plane. Unequal current flow on the two ground planes unbalances the stripline and excites a parallel-plate mode between the ground planes. Waveguide wall slots also excite higher-order modes, but these cannot propagate because they are below their cutoff frequencies. The parallel-plate mode is another TEM mode with no low-frequency cutoff. Power in this mode propagates away from the slot and couples into the other slots in an undesirable manner or radiates from edges.

Shorting pins between the two ground planes contain the parallel-plate mode around the slot. By placing the rows of pins parallel with the axis of the slot and a quarter wavelength away from the slot, the rows of pins reflect an open-circuit impedance at the slot. The side rows of pins complete the box and convert the parallel-plate mode into a waveguide TE_{10} mode. The box formed by the rows of shorting pins and the two ground planes form a resonant cavity in shunt with the slot admittance. The resonant cavity places a standing-wave current null on a centered slot and does not excite it. Only the normal stripline currents feed the slot.

From an impedance point of view, the cavity is a second parallel resonant circuit that increases the stored energy of the antenna. Q increases and bandwidth decreases. Because only a portion of the available power would be converted to the parallel-plate mode by the slot discontinuity, we analyze the cavity as a circuit coupled through a transformer to the input. The transformer increases the impedance of the resonant cavity at the input and controls the division of power between the slot and
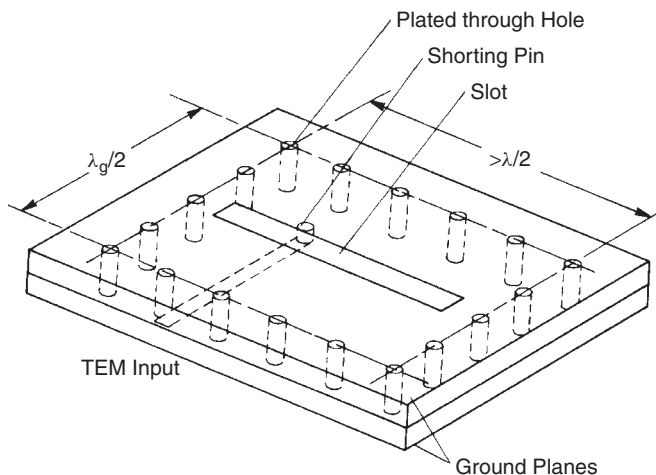

FIGURE 5-55   Stripline series slot.

the cavity. The cavity reactance slope limits the bandwidth of the stripline-fed slot to a few percent. Increasing the impedance of the waveguide cavity transmission line reduces the reactance slope contributed by the cavity. We increase the bandwidth by using greater distances between the ground planes and thereby increase the waveguide transmission-line impedance. In general, greater volumes for an antenna increase the impedance bandwidth.

Rotating the slot relative to the stripline feeding line reduces its load on the transmission line. The waveguide top wall series slot relation [Eq. (5-34)] applies in this case. The slot maintains its polarization while the nonradiating stripline center conductor approaches the slot at an angle. Rotated slots in waveguide must be paired symmetrically to reduce cross-polarization. A longitudinal array [37] can be made by placing all the slots on the centerline of a boxed stripline. Either edge plating or a series of plated-through holes forms a waveguide structure that supports only the TE_{10} mode. Slots placed on the centerline (as in Figure 5-59, slot c) fail to interrupt the waveguide mode currents. The stripline meanders below and varies the excitation by changing the angle between the slot and the stripline center conductor. The slight loading of each slot excites very little of the parallel-plate mode that causes unwanted slot coupling. Both traveling-wave and resonant linear arrays are possible. See Section 5-26 for a discussion of slot arrays.

5-22 SHALLOW-CAVITY CROSSED-SLOT ANTENNA

We can feed the slot in Figure 5-55 by exciting the cavity in an odd mode from two points on opposite sides of the slot. To be able to excite both polarizations, we divide the slot in two and rotate the two parts in opposite directions by $45°$ to form a cross. We use a square cavity to maintain symmetry and replace the shorting pins with solid walls (Figure 5-56c). Since we feed across the diagonal between the crossed slots, we excite both slots. The sum of the fields radiated from the two slots is polarized in the direction of the diagonal. We increase the radiation conduction by lengthening the crossed slots to the maximum, which lowers the Q (increased bandwidth). The cavity compensates for the slot susceptance to obtain resonance. A crossed-slot antenna was built [38] with the following dimensions:

Cavity edge	0.65λ
Cavity depth	0.08λ
Slot length	0.915λ

The measured $2:1$ VSWR bandwidth was 20.8%. The bandwidth exceeded that of a microstrip patch of the same thickness by about $\sqrt{2}$. Lindberg [39] found that the resonant length of the slot depends on the cavity depth and requires some experimental adjustment.

King and Wong [41] added ridges (Figure 5-56b) to increase the bandwidth. Antennas with ridges need a larger cavity width and a longer slot than the unridged design. The ridges can be stepped as shown to increase the bandwidth. Adding ridges gives us extra parameters to adjust for best input match performance. The following design with uniform ridges produces a 58.7% $2.5:1$ VSWR bandwidth with a double resonance curve.
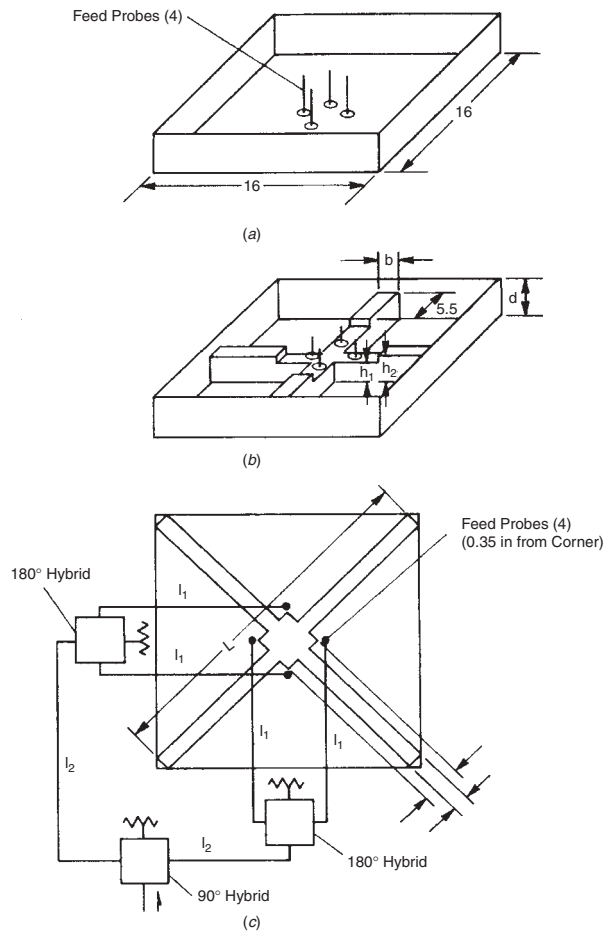
FIGURE 5-56   Shallow-cavity crossed-slot antenna: (*a*) cavity with ridge; (*b*) cavity with ridge; (*c*) typical slot configuration. All dimensions are in inches. (From [38], Fig. 2, © 1975 IEEE.)

Cavity edge	0.924λ	Slot width, W_2	0.058λ
Slot length	1.3λ	Ridge height	0.076λ
Ridge width	0.087λ	Feed width, W_1	0.144λ
Cavity thickness	0.115λ		

Both the ridge and slot shapes can be varied to improve the performance. As fed in Figure 5-56*c*, the antenna radiates circular polarization on a boresight. Near the horizon (90° from the boresight), the polarization reduces to linear as we enter the null of one of the slots.

5-23   WAVEGUIDE-FED SLOTS [24, p. 291; 40, p. 95]

Waveguide is an ideal transmission line for feeding slots. Although its impedance cannot be defined uniquely, all possible candidates—voltage and current, power and

current, or power and voltage—yield high values that match the high values of impedance of half-wavelength slots. Waveguide provides a rigid structure with shielded fields. The slots couple to the internal fields and allow the easy construction of linear arrays fed from traveling waves or standing waves in the waveguide. By controlling the position of the slots in the walls, the amplitude of the slot excitation can be controlled.

The waveguide fields excite a slot when the slot interrupts the waveguide wall currents. When excited, the slot loads the waveguide transmission line. We make the following assumptions about the wall slots.

1. The slot width is narrow. When a slot grows in width, we must either consider it to be an aperture in the wall or assume that it is excited by interrupting currents in two coordinate directions.
2. The slot is a resonant length and its length is near $\lambda/2$. The waveguide environment, the wall thickness, and the position in the wall all affect the resonant length. In most cases, experiments must determine the resonant length.
3. The electric field is directed across the narrow width of the slot and varies sinusoidally along its length and is independent of the excitation fields. This reiterates assumptions 1 and 2. An aperture radiates the polarization of the incident fields, but resonant-length slots can be excited only with a sinusoidal voltage standing wave. The slot direction determines polarization.
4. The waveguide walls are perfectly conducting and infinitely thin. Even though the walls have thickness, the difference has a small effect on the general form of the slot excitation formulas. As in the case of the resonant length, experiments determine a few values from which the rest must be interpolated, or the values provide the constants for more elaborate models.

5-24   RECTANGULAR-WAVEGUIDE WALL SLOTS

The lowest-order mode (TE_{10}) in a rectangular waveguide has the following fields [41, p. 69]:

$$E_y = E_0 \sin(k_c x)e^{-jk_g z}$$

$$H_x = -\frac{k_g E_0}{\omega\mu} \sin(k_c x)e^{-jk_g z} \tag{5-24}$$

$$H_z = -\frac{k_c E_0}{j\omega\mu} \cos(k_c x)e^{-jk_g z}$$

where $k_c = \pi/a$, $k_g^2 = k_c^2 - k^2$, and a is the guide width with cutoff wavelength $\lambda_c = 2a$. We can separate TE_{10}-mode rectangular waveguide fields into two plane waves that propagate at an angle to the axis and reflect from the two narrow walls. We denote as ξ the angle of the waves measured from the centerline of the waveguide or with respect to the wall. We relate the waveguide propagation to this angle:

$$\xi = \sin^{-1}(\lambda/\lambda_c) \tag{5-25}$$

At high frequencies, $\xi \to 0$ and the waves travel straight through the guide as though the walls are not there. As the wavelength approaches cutoff, $\xi \to 90°$ and the waves

reflect back and forth between the sidewalls instead of propagating down the guide. This angle factors into the expressions for slot loading to the waveguide transmission line and can be related to propagation:

$$\text{guide wavelength, } \lambda_g = \frac{\lambda}{\cos \xi} = \frac{\lambda}{\sqrt{1 - (\lambda/\lambda_c)^2}}$$

$$\text{phase velocity } V_{\text{ph}} = \frac{c}{\cos \xi} \quad \text{and} \quad \text{group velocity} = c \cos \xi$$

$$\text{relative propagation constant } P = \frac{\lambda}{\lambda_g} = \cos \xi$$

For analysis we divide the fields bouncing down the waveguide into z-directed fields of the axial wave moving down the guide and x-directed fields of the transverse wave, a standing wave between the two narrow walls. A standing wave causes a $90°$ separation of the voltage and currents in a transmission line as shown in Figure 5-1. The phase of the currents excited in the waveguide walls due to the fields will be $90°$ relative to the electric field.

The wall currents $\mathbf{J}_s$ are determined by $\mathbf{J} = \mathbf{n} \times \mathbf{H}$, where $\mathbf{n}$ is the unit normal to the wall. When we apply this boundary condition to the walls, we obtain the following wall currents:

Sidewalls:

$$J_y = -j\frac{E_0 k_c}{\omega\mu}e^{-jk_g z}$$

Bottom wall ($y = 0$):

$$J_s = \frac{E_0}{\omega\mu}e^{-jk_g z}[k_g \sin(k_c x)\hat{\mathbf{z}} + jk_c \cos(k_c x)\hat{\mathbf{x}}] \tag{5-26}$$

Top wall ($y = b$):

$$J_s = \frac{-E_0}{\omega\mu}e^{-jk_g z}[k_g \sin(k_c x)\hat{\mathbf{z}} + jk_c \cos(k_c x)\hat{\mathbf{x}}]$$

Equation (5-26) shows that transverse wave currents are $90°$ out of phase with respect to the electric field E_0. The current alternates between the two types of current as the wave propagates down the waveguide. In the case of a standing wave along the z-axis caused by a short circuit, the axial wave currents are $90°$ out of phase with the electric field across the waveguide (Figure 5-1). The peak amplitude of the transverse wave currents occurs at the same point as the electric field in a standing wave along the z-axis, since both are $90°$ out of phase with the axial wave currents. The sidewalls J_y have only transverse wave currents. The top and bottom broad walls have both x-directed transverse wave and z-directed axial wave currents. Figure 5-57*a* shows the direction and amplitude distribution of these transverse waves. Slots interrupting these
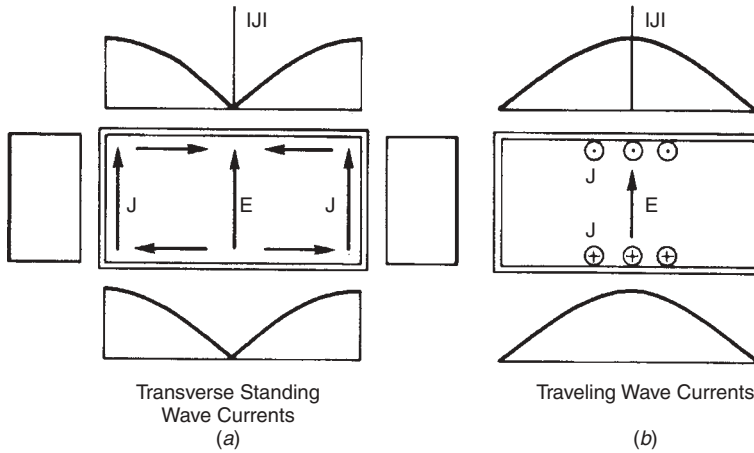
FIGURE 5-57 TE$_{10}$-mode rectangular waveguide wall currents: (*a*) transverse wave currents; (*b*) axial wave currents.
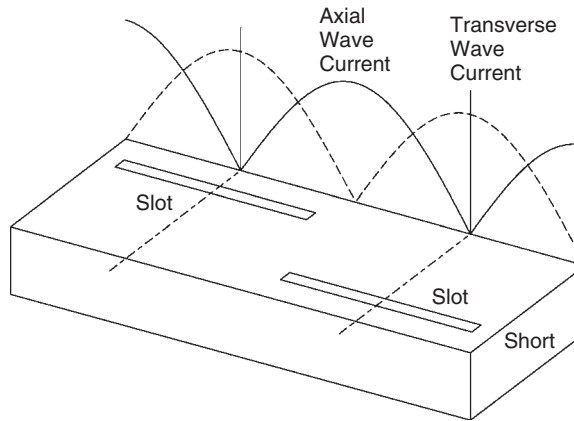

FIGURE 5-58 Short-circuited waveguide axial and transverse wave currents and the location of longitudinal wall slots.

currents are shunt loads to the waveguide. In an axial wave along the z-axis, these transverse waves propagate in the z-axis direction.

Equation (5-26) shows that the transverse wave currents are $90°$ phase with respect to the axial wave currents. Figure 5-58 shows the two types of currents along the z-axis when the guide has a short circuit at its end. When measuring slots that interrupt transverse wave currents, we need to place the waveguide short at $\lambda_g/4$ or $3\lambda_g/4$ away from the slot. This locates the peak of the transverse wave currents flowing around the waveguide walls at the slot shown in Figure 5-58 because the axial wave currents are at a minimum. The second consideration is the shunt load on the waveguide. The $\lambda_g/4$ section of waveguide transforms a short circuit on the end of the waveguide (to the axial wave currents) to an open circuit at the slot. From a voltage point of view the susceptance of the shorted stub is at a minimum. We place the short circuit at

$\lambda_g/2$ from the last slot for a series loading slot that interrupts the axial wave currents. This locates the current maximum at the slot and causes maximum interaction with the waveguide fields. Figure 5-58 illustrates the placement of the next slot $\lambda_g/2$ down the guide at the next current maximum. Figure 5-57a indicates the transverse wave current flow and we see that the currents flow toward the centerline, producing currents 180° out of phase on the two sides of the centerline. The two slots in Figure 5-58 are excited by oppositely directed currents that add 180° phase shift between the slots. This phase shift compensates for internal standing-wave current phasing of 180° due to the $\lambda_g/2$ spacing.

Longitudinal top and bottom wall slots cut x-directed transverse shunt currents. The central slot c, located at a current null, fails to be excited. We use this nonradiating slot to insert a traveling probe to measure VSWR. When moved off center, slots d and e cut x-directed currents and are excited. The shunt conductance has the relation

$$g = g_1 \sin^2 \frac{\pi x'}{a} \qquad (5\text{-}27)$$

where x' is the distance from the guide centerline. Shunt currents on either side of the centerline of the top or bottom wall (Figure 5-57a) have different directions. Besides any traveling-wave phase, slots d and e (Figure 5-59) are 180° out of phase. Top-wall longitudinal slots generate no cross-polarization, since all maintain the same orientation. We relate the peak conductance g_1 to the direction of the waves in the guide [41]:

$$g_1 = 2.09 \frac{a}{b} \frac{\cos^2[(\pi/2)\cos\xi]}{\cos\xi} \qquad (5\text{-}28)$$

Equation (5-28) indicates that the conductance increases for a given spacing off the centerline as the frequency approaches cutoff and $\xi \to \pi/2$.

We cannot use Eqs. (5-27) and (5-28) for design because they do not include the wall thickness and we need to determine the exact length for resonance. The resonant length depends on the spacing from the centerline. Fortunately, the coupling between longitudinal slots is small enough that measurements can be made on single slots. Elliott suggests a measurement plan for longitudinal slots [3]. We build a series of slotted waveguides each containing a single slot at different distances from the centerline. Seven cases are sufficient to generate a curve for design. We need
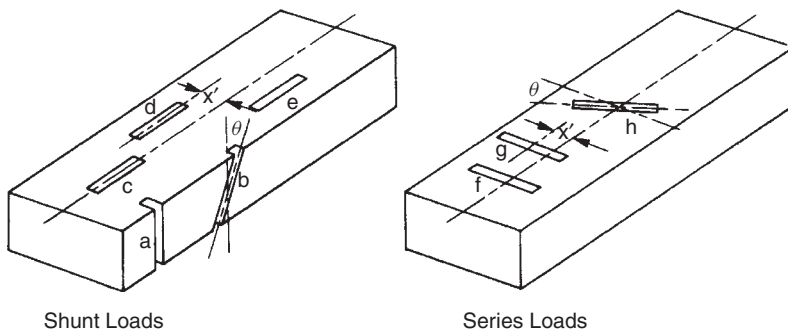

Shunt Loads   Series Loads

FIGURE 5-59   TE$_{10}$-mode rectangular waveguide wall slots.

to locate a sliding short circuit farther down the waveguide and adjust it until the standing-wave current peaks at the slot to produce maximum radiation and conductance. With a network analyzer we measure the conductance normalized with respect to the waveguide impedance. Initially, we machine the slots too short, measure the results, and then machine longer slots using the same guides and remeasure until they pass through resonance.

Since the manufacturing cost of test slots is high and they require careful measurements, analytical methods of determining slot parameters become attractive. FEM programs can model the details of the slot, the waveguide, and the wall thickness. A number of runs similar to those of the measurements allows design curves to be created.

Sidewall slots (Figure 5-59) interrupt shunt transverse waves. Slot a fails to cut surface currents and is not excited. By tilting slot b, currents are cut. The sidewall slot conductance is given for $\theta < 30°$ by

$$g = g_0 \sin^2 \theta \tag{5-29}$$

where g_0 is the peak conductance. Note that the sidewall slots must cut into the top and bottom walls to achieve a resonant length. The peak conductance can be related to the direction of the waves in the waveguide [Eq. (5-25)] [1, p. 82]:

$$g_0 = 2.09 \frac{a \sin^4 \xi}{b \cos \xi} \tag{5-30}$$

Equation (5-30) shows the relationship of the slot load conductance versus the frequency. As frequency increases, ξ decreases and the conductance falls off as the fourth power of the sine of the angle. The complete theory of Stevenson gives the conductance for an arbitrary tilt [42]:

$$g = 2.09 \frac{a \sin^4 \xi}{b \cos \xi} \left[\frac{\sin \theta \cos[(\pi/2) \cos \xi \sin \theta]}{1 - \cos^2 \xi \sin^2 \theta} \right]^2 \tag{5-31}$$

Tilting the slots to interrupt currents introduces cross-polarization components in the array pattern. We alternate the direction of tilt to reduce cross-polarization. Two things prevent the total cancellation of cross-polarization. First, the amplitude taper of the array changes the amplitude from element to element and the fields do not cancel. Alternating the tilt of the slots symmetrically about the centerline in an array with an even number of elements prevents cross-polarization on the boresight. Off the boresight, the array effect of the spaced elements introduces a cross-polarization pattern, since cross-polarization is not canceled at each element.

Although Eqs. (5-29) and (5-30) give the slot conductance, they cannot be used for design. They assume an infinitely thin wall and ignore the high level of radiation along the waveguide wall. These slots readily couple to neighboring slots. The effective conductance needs to include the mutual conductance. For these slots we build a series of slotted waveguides containing a group of slots all tilted to the same angle and cut so that they are a resonant length. This means that we will first need to build the slots about 5% shorter than resonance length, make measurements, and then machine the slots longer and repeat the measurements to find the resonant length. We space the slots at the same distance as will be used in the final design and either place a

short-circuit beyond the last slot to produce a maximum current at all slots or load the waveguide to form a nonresonant array. We measure the load of the group of slots on the waveguide transmission line using a network analyzer and divide the conductance by the number of slots to get an incremental conductance. This conductance is larger than the one measured on a single slot. We fit the group of measurements to a curve that replaces Eq. (5-29) for design.

Axial z-directed waves (Figure 5-57b) peak in the center of the broad walls and taper to zero at the edges. They remain zero on the sidewalls. When centered, transverse slots f and g (Figure 5-59) interrupt the maximum current. When moved off center, g, their series loading to the waveguide drops:

$$R = R_0 \cos^2 \frac{\pi x'}{a} \tag{5-32}$$

The maximum resistance is related to the direction of the waves in the waveguide:

$$R_0 = 2.09 \frac{a}{b} \frac{\sin^2 \xi}{\cos^3 \xi} \cos^2 \left(\frac{\pi}{2} \sin \xi \right) \tag{5-33}$$

An evaluation of Eq. (5-33) shows that the resistance increases as frequency approaches cutoff for a given location of the slot, a result similar to that for other slot configurations. The mutual coupling between these series slots is high. We perform incremental resistance experiments similar to the procedure used for sidewall slots to discover the true values of resistance versus offset.

Rotating the broadwall transverse slot, h, reduces the z-axis directed current interrupted. When the slot is centered, equal and opposite shunt currents are cut by the slot and the slot fails to present a load to shunt currents:

$$R = R_0 \cos^2 \theta \tag{5-34}$$

We can excite slots a and c by probe coupling into the waveguide. A probe placed next to the slot and extending into the guide feeds the slot. The longer the probe, the more it disturbs the waveguide fields to excite the slot. Probes placed on opposite sides of the slots induce fields $180°$ out of phase with respect to each other.

5-25   CIRCULAR-WAVEGUIDE SLOTS

Figure 5-60 shows the transverse wave and axial wave currents of the circular waveguide TE_{11} dominant mode. Slots may be placed successfully only at the current maximums without affecting the polarization of the internal wave. A longitudinal slot placed halfway between the current maximums, $45°$, interrupts only shunt transverse waves. Since any polarization is possible in the circular waveguide, analytically we divide the incident wave into two waves. One is polarized in the direction of the slot; the other is polarized perpendicular to the slot axis. The wave polarized perpendicular to the slot location has its current maximum at the slot and it removes power from the wave. The other wave produces a current null on the slot. When we combine the two fields after the slot, the unloaded wave is larger and the combined wave rotates its polarization toward the slot. Circumferential slots interrupting axial wave currents
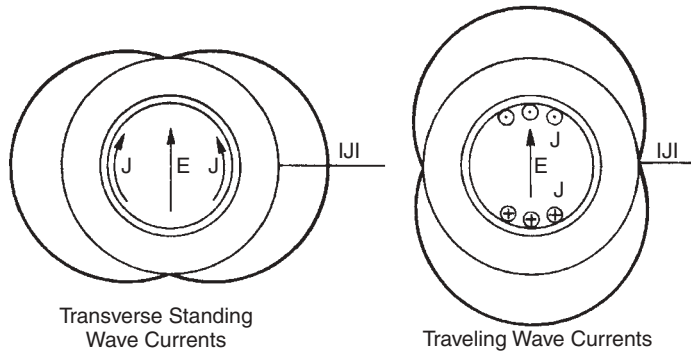
FIGURE 5-60 TE_{11}-mode circular waveguide wall currents.

also cause polarization rotation of the wave when not centered $90°$ from the electric field direction.

Slots placed at the maximum of transverse currents cut them when rotated about the axis of the waveguide. Like rectangular-waveguide sidewall slots, the slots oriented perpendicular to the guide axis, circumferential, do not load the waveguide. Rotating the slot increases the shunt load on the waveguide. Slots placed at the maximum of the axial wave cut z-directed currents. Field probes can monitor the internal fields of the waveguide through a longitudinal slot without causing radiation from the slot. When the slot is rotated away from the axis direction, it interrupts series axial wave currents, loads the waveguide, and radiates.

Coaxial TEM-mode transmission line and TM_{01}-mode circular waveguide have the same outer wall currents (Figure 5-61). Slots can be excited and load the waveguide only by interrupting these axial wave currents. In Figure 5-61, slot a fails to cut currents and is not excited. VSWR measuring probes use this slot. Slots b and c interrupt the currents and series-load the guide. Slot c, whose total length is resonant, is excited by the small portion in the center cutting z-directed currents. We can probe feed slot a, but the probe shunt loads the waveguide or TEM coax that would be series loads on the waveguide if they directly interrupted the axial wave currents.
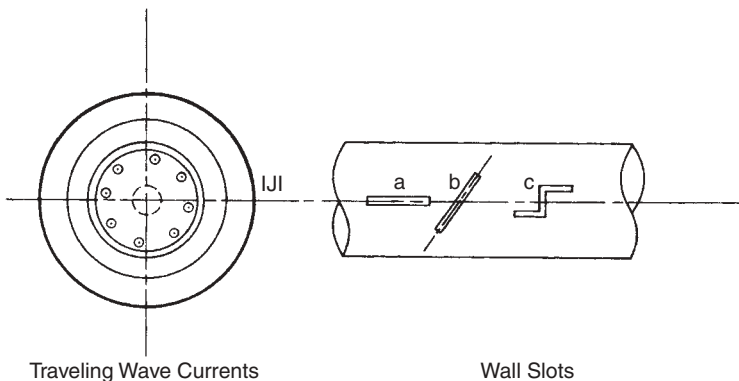

FIGURE 5-61   Coax or TM_{01}-mode circular waveguide wall currents and slots.

5-26   WAVEGUIDE SLOT ARRAYS [4, p. 402]

Waveguide slot arrays can produce low sidelobe antennas for pencil beams with good aperture efficiency. Array fabrication requires close manufacturing tolerances to achieve the desired amplitude distribution because random errors in manufacture produce unwanted sidelobes and raise the general sidelobe level. Producing these arrays is an art requiring careful analysis of all slot interactions, slot dimensioning determined from models and measurements, and precision machining and assembly.

An array consists of a set of waveguides loaded with slots and joined with a corporate feed into the total array. The corporate feed can also be a slotted array feeding the individual waveguides that contain the radiating slots. Aperture size and distribution determine the beamwidth and sidelobes in the various planes. We divide arrays of slots into two groups: nonresonant, excited by traveling waves, and resonant, excited by standing waves. Waves either travel along the guide into a terminating load or reflect from a short and set up standing waves along the z-axis (Figure 5-58). Traveling-wave currents excite the slots as they pass, and slots may be placed anywhere relative to the load. The distance between slots and the propagation constant determine the relative phases. Standing waves set up a fixed sinusoidal current pattern along the waveguide axis at a given frequency. The standing-wave phase is either $0°$ or $180°$. Slots placed in the current nulls of standing waves interrupt no currents and fail to be excited by the waveguide. We can vary the amplitude by the z-axis placement of the slots. The termination determines the array type. Do not confuse transverse waves that produce shunt currents and z-axis standing waves caused by a short-circuit termination. Both traveling and standing waves on the z-axis have shunt currents.

Standing waves (resonant array) produce beams normal to the array axis. A resonant array maintains its beam direction when frequency changes, but the standing-wave pattern shifts and changes the excitation of the slots (Figure 5-62). The amplitudes of the slots farthest from the short circuit change the most, since the standing waves have shifted farther. The length of the resonant array determines its bandwidth. The pattern shape changes because distribution and input impedance change as the loads change when the standing-wave currents shift.

Nonresonant array (traveling-wave) beam directions are functions of the propagation constant of the wave exciting the slots. Changing the frequency shifts the beam direction. If the load on the end reflects a wave, another beam forms from the reflected traveling wave. The second beam appears at the same angle to the axis of the waveguide
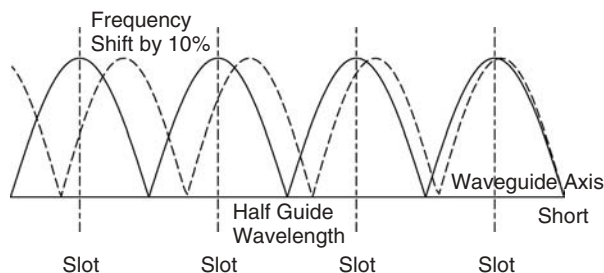

FIGURE 5-62   Standing-wave currents in resonant array relative to slots and after 10% frequency shift.

as the first but measured from the $-z$-axis. The first-pass radiated power and return loss of the load determine the level of this second beam relative to the first.

Both resonant and nonresonant waveguide slot arrays use resonant-length slots. We space the slots $\lambda_g/2$ apart in the resonant array, as shown in Figure 5-58. We place the slots at alternating positions about the centerline of the broadwall or at alternating tilt angles in the sidewall to give the additional $180°$ phase shift to produce a broadside beam. The admittances of the slots of the resonant array add at the input because the $\lambda_g/2$ spacing produces a complete rotation around the Smith chart. In nonresonant arrays a traveling wave is used to excite the slots. We space the slots at other than $\lambda_g/2$ distances and terminate the waveguide with a load. We assume a matched system throughout the antenna in a first-order analysis suitable for most designs. The beam of most nonresonant slot arrays is designed to backfire at an angle to broadside.

5-26.1 Nonresonant Array [43]

In a nonresonant waveguide, slot array resonant-length slots are used in a traveling-wave antenna terminated at the end with a load. The antenna radiates at an angle to the normal of the waveguide face determined by wave velocity and slot spacing. We vary the slot loading along the waveguide so that each slot radiates the proper amount of the remaining power. A termination absorbs the power remaining after the last slot. With a mismatched termination the reflected power radiates a second lower-amplitude beam as the wave travels to the source.

We design with either shunt- or series-loading slots. A shunt slot radiates the power $|V|^2 g_i/2$, where g_i is the normalized slot conductance. Similarly, a series slot radiates the power $|I|^2 r_i/2$, where r_i is the normalized slot resistance. We normalize the conductance or resistance to a per unit length function: $g(z)$ or $r(z)$. The attenuation equation (4-78) becomes

$$\frac{1}{P(z)}\frac{dP}{dz} = -g(z) \quad \text{or} \quad -r(z) \tag{5-35}$$

Equation (5-35) modifies the normalized attenuation equation (4-79) [24, p. 291]:

$$g(z)L = \frac{|A(z)|^2}{[1/(1-R)]\int_0^L |A(z)|^2\,dz - \int_0^z |A(z)|^2\,dz} \tag{5-36}$$

where the aperture runs $\pm L/2$ and R is the ratio of the input power absorbed by the termination. $A(z)$ is the normalized aperture distribution on the interval $\pm\frac{1}{2}$. We change to $r(z)L$ in Eq. (5-36) for series-loading slots.

Equation (5-36) assumes light loading by the slots so that the waveguide transmission line is matched at all points. This approximation improves as the length increases. Equation (5-36) is the same as Eq. (4-79) except for a constant. We divide the values in Table 4-28 or Figure 4-26 by 4.34 to calculate normalized conductance (resistance) of shunt (series) slots times the array length. Each slot provides the loading over the spacing between slots:

$$g_i = \int_{-d/2}^{d/2} g(z)\,dz \simeq g(z_i)\,d$$

where d is the spacing of the slot at z_i.

We space the slots at other than $\lambda_g/2$. At $\lambda_g/2$ spacings, all reflections from the mismatches (slots) add in phase at the input. The small mismatches from each slot add with various phase angles for element spacing different from $\lambda_g/2$ and cancel each other to some extent to give a good input match over a reasonable bandwidth. When we increase the array length, we can no longer ignore the waveguide losses. The slot conductances become very small and radiate power on the same order as the losses. We modify Eq. (5-36) to include the losses as in Eq. (4-79), and the slot conductance increases to compensate for the ohmic losses in the walls. A small slot conductance is difficult to achieve with longitudinal broadwall slots because one edge of the slot must be over the centerline of the waveguide wall and the results become unpredictable. The achievable conductances limit possible distributions in a slotted waveguide array. Mutual coupling between slots changes the distribution and we must modify the slot offsets to account for mutual coupling using Eq. (3-23).

If we specify the radiating power of each slot in a discrete sequence P_i, we modify Eq. (5-36). The integrals become summations, since

$$|A(z)|^2 = \delta(z - id)P_i$$

where d is the slot spacing, $\delta(x)$ the Dirac delta (impulse) function, and P_i the power coefficient of the ith slot. The power radiated is

$$\sum_{i=1}^{N} P_i = P_{\text{in}}(1 - R) = \int_0^L |A(z)|^2\, dz$$

The integral $\int_0^z |A(z)|^2\, dz$ is the power radiated by the preceding slots. Equation (5-36) reduces to

$$g_i = r_i = \frac{P_i}{1 - \sum_{n=1}^{i-1} P_n} \tag{5-37}$$

Dissipating more power in the termination decreases each P_i and the required conductance (resistance) range of the slots.

We alternate the locations of longitudinal slots about the centerline of the broadwall to add $180°$ phase shift between elements. Similarly, sidewall slot directions are alternated along the array. The additional phase shifts cause backfire of the beam in most cases. The element spacing, as well as the traveling-wave phase velocity, determines the beam direction. The phasing equation in the array factor for beam peak becomes $kd\cos\theta + 2n\pi = Pkd - \pi$, where θ is measured from the array axis, P is the relative propagation constant ($P < 1$), and n is an arbitrary integer. We solve for the beam peak direction and the necessary spacing to get a particular beam direction:

$$\theta = \cos^{-1}\left[P - \frac{(n + \frac{1}{2})\lambda}{d} \right] \tag{5-38}$$

$$\frac{d}{\lambda} = \frac{n + \frac{1}{2}}{P - \cos\theta_{\text{max}}} \tag{5-39}$$

We usually work with $n = 0$ because using $n > 0$ produces multiple beams.

Example   Compute slot spacing to produce a beam at $\theta = 135°$ in a waveguide of width 0.65λ. Calculate the relative propagation constant from the general equation for a waveguide.

$$P = \sqrt{1 - \left(\frac{\lambda}{\lambda_c}\right)^2}$$

For $\lambda_c = 2a$,

$$P = \sqrt{1 - \left(\frac{1}{1.3}\right)^2} = 0.640 = \frac{\lambda}{\lambda_g}$$

From Eq. (5-39), using $n = 0$, we determine spacing in free space: $d/\lambda = 0.371$. The waveguide spacing is given by

$$\frac{d}{\lambda_g} = \frac{d}{\lambda}P = 0.371(0.640) = 0.237$$

If we use $n = 1$, then $d/\lambda = 1.11$, which radiates an additional beam at $\theta = 79°$ for $n = 0$ [Eq. (5-38)].

Beams enter visible space at $\cos\theta = -1$ (180°) and move toward end fire ($\theta = 0$) as the spacing increases. We calculate the region of single-beam operation from Eq. (5-39). The minimum d/λ occurs when $\theta = 180°$ for $n = 0$, and the maximum occurs when $\theta = 180°$ for $n = 1$:

$$\frac{0.5}{1 + P} \leq \frac{d}{\lambda} \leq \frac{1.5}{1 + P} \tag{5-40}$$

We substitute the upper bound into Eq. (5-38) and use $n = 1$ to derive the minimum angle of single-beam operation:

$$\theta_{\min} = \cos^{-1}\left(P - \frac{1 + P}{3}\right) \tag{5-41}$$

Example   Determine the minimum scan angle (toward end fire) for $P = 0.6, 0.7, 0.8,$ and 0.9 that has a single beam. We substitute these values into Eq. (5-41) to find:

P	0.6	0.7	0.8	0.9
$\theta_{\min}$	86.2°	82.3°	78.5°	74.5°

If we scan to $\theta = 90°$, the spacing becomes $\lambda_g/2$ and the mismatches from each slot add to the input and produce a resonant array. The array with a forward firing beam has a slot spacing greater than $\lambda_g/2$. Given a waveguide with $P = 0.8$, we use Eq. (5-39) to calculate spacing to give beams at 80° and 100°:

$$\frac{d}{\lambda} = \frac{0.5}{0.8 - \cos 80°} = 0.798 \quad \text{and} \quad \frac{d}{\lambda} = \frac{0.5}{0.8 - \cos 100°} = 0.514$$

$$\frac{d}{\lambda_g} = \frac{d}{\lambda}P = 0.639 \quad \text{and} \quad \frac{d}{\lambda_g} = \frac{d}{\lambda}P = 0.411$$

A nonresonant array has a backfire beam that scans toward broadside as frequency (and P) increases. Hansen [44, p. 90] gives the slope of the beam shift with frequency change:

$$f \frac{d \sin \theta}{df} = \frac{1}{P} - \sin \theta \qquad (5\text{-}42)$$

where f is the frequency.

5-26.2 Resonant Array

We space the slots at $\lambda_g/2$ and terminate the waveguide end with a short circuit either $\lambda_g/4$ or $3\lambda_g/4$ from the last one for shunt loading slots in a resonant array. The beam radiates broadside to the array. The 2:1 VSWR bandwidth of the array is approximately 50%/N for N elements in the array. The antenna is narrowband. The admittances of all elements add at the input. To have a matched input, $\sum_{i=1}^{N} g_i = 1$, where g_i is the normalized slot conductance. If we define P_i as the normalized power radiated by the ith slot, then

$$g_i = P_i \qquad \text{where} \quad \sum_{i=1}^{N} P_i = 1$$

5-26.3 Improved Design Methods

The methods given above ignore the interaction of slots and their effect on the transmission line. We can describe the array as a loaded transmission line and consider the interactions of the slots by accounting for the transmission-line mismatches [45, pp. 9–11]. We ignore the mutual coupling for longitudinal broadwall slots because it is small, but sidewall slots have high mutual coupling and require an adjustment of the effective slot impedance. We use an incremental admittance, found from the measured change in admittance, when one slot is added to the array or total conductance of the array divided by the number. This accounts somewhat for the mutual coupling.

Elliott and Kurtz [46] relate the self-admittance of a longitudinal broad-wall slot, measured or calculated, to the mutual admittance of the array of slots found from equivalent dipoles. They use Babinet's principle and the mutual impedance of equivalent dipoles. The method requires solution of a set of $2N$ equations in the location and length of the slots to give the desired excitation while accounting for mutual coupling. Their formulation ignores slot interaction in the waveguide beyond the first-order mode. Elliott [47] extends this method to the analysis and design of nonresonant arrays. Of course, when we design a planar array, the slots between waveguide sticks couple readily and we need to account for the mutual coupling between them. The voltage excitation needs to be adjusted to account for this coupling or the desired distribution will not be achieved.

Dielectric loaded waveguide arrays require additional analysis because the approximation of a piecewise sinusoidal distribution, such as dipole current, fails to model the slot distribution adequately. Elliott [48] uses a slot distribution

$$E(x) = \cos \frac{\pi x}{2b}$$

where b is the length. Mutual impedances between dipoles that have the wrong distribution are not used; instead, the active admittances are found from forward and

back scattering between the slots directly. The method still requires the solution of $2N$ equations for the slot lengths and locations.

REFERENCES

1. R. F. Harrington, *Time-Harmonic Electromagnetic Fields*, McGraw-HiIl, New York, 1961.

2. C. A. Balanis, *Antenna Theory, Analysis and Design*, 2nd ed., Wiley, New York, 1997.

3. H. G. Booker, Slot aerials and their relation to complementary wire aerials, *Proceedings of IEE*, vol. 92, pt. IIIA, 1946, pp. 620–626.

4. R. S. Elliott, *Antenna Theory and Design*, Prentice-Hall, Englewood Cliffs, NJ, 1981.

5. V. H. Rumsey, *Frequency Independent Antennas*, Academic Press, New York, 1966.

6. W. H. Watson, *Wave Guide Transmission and Antenna Systems*, Oxford University Press, London, 1947.

7. R. W. Masters, Super-turnstile antenna, *Broadcast News*, vol. 42, January 1946.

8. J. D. Kraus, *Antennas*, McGraw-Hill, New York, 1950.

9. H. M. Elkamchouchi, Cylindrical and three-dimensional corner reflector antennas, *IEEE Transactions on Antennas and Propagation*, vol. AP-31, no. 3, May 1983, pp. 451–455.

10. S. Maci et al., Diffraction at artificially soft and hard surfaces by using incremental diffraction coefficients, *IEEE AP-S Symposium*, 1994, pp. 1464–1467.

11. E. L. Bock, J. A. Nelson, and A. Dome, *Very High Frequency Techniques*, McGraw-Hill, New York, 1947. Chapter 5.

12. A. J. Poggio and P. E. Mayes, Pattern bandwidth optimization of the sleeve monopole antenna, *IEEE Transactions on Antennas and Propagation*, vol. AP-14, no. 5, September 1966, pp. 623–645.

13. W. L. Stutzman and G. A. Thiele, *Antenna Theory and Design*, Wiley, New York, 1981.

14. H. E. King and J. L. Wong, An experimental study of a balun-fed open-sleeve dipole in front of a metallic reflector, *IEEE Transactions on Antennas and Propagation*, vol. AP-19, no. 2, March 1972, pp. 201–204.

15. J. L. Wong and H. E. King, A cavity-backed dipole antenna with wide bandwidth characteristics, *IEEE Transactions on Antennas and Propagation*, vol. AP-21, no. 5, September 1973, pp. 725–727.

16. A. Kumar and H. D. Hristov, *Microwave Cavity Antennas*, Artech House, Boston, 1989.

17. Y. Mushiake, An exact step-up impedance ratio chart of folded antenna, *IRE Transactions on Antennas and Propagation*, vol. AP-2, 1954, p. 163.

18. R. C. Hansen, Folded and T-match dipole transformation ratio, *IEEE Transactions on Antennas and Propagation*, vol. AP-30, no. 1, January 1982, pp. 161–162.

19. *The ARRL Antenna Book*, American Radio Relay League, Inc., Newington, CT, 1974.

20. R. A. Burberry, *VHF and UHF Antennas*, Peter Peregrinus, London, 1992.

21. N. Marchand, Transmission-line conversion transformers, *Electronics*, December 1941, pp. 142–145.

22. W. L. Weeks, *Antenna Engineering*, McGraw-Hill, New York, 1968.

23. W. K. Roberts, A new wide-band balun, *Proceedings of IRE*, vol. 45, December 1957, pp. 1628–1631.

24. S. Silver, ed., *Microwave Antenna Theory and Design*, McGraw-Hill, New York, 1949.

25. J. W. Duncan and V. P. Minerva, 100 : 1 Bandwidth balun transformer, *Proceedings of IRE*, vol. 48, February 1960, pp. 156–164.

26. B. A. Munk, Baluns, Chapter 23 in J. D. Kraus and R. J. Marhefka, *Antennas*, McGraw-Hill, New York, 2002.

27. P. K. Park and C. T. Tai, Receiving antennas, Chapter 6 in Y. T. Lo and S. W. Lee, eds., *Antenna Handbook*, Van Nostrand Reinhold, New York, 1993.

28. A. Alford and A. G. Kandoian, Ultrahigh frequency loop antennas, *AIEE Transactions,* vol. 59, 1940, pp. 843–848.

29. A. J. Fenn, Arrays of horizontally polarized loop-fed slotted cylinder antennas, *IEEE Transactions on Antennas and Propagation,* vol. AP-33, no. 4, April 1985, pp. 375–382.

30. T. Tsukiji and S. Tou, On polygonal loop antennas, *IEEE Transactions on Antennas and Propagation*, vol. AP-28, no. 4, July 1980, p. 571.

31. W. C. Wilkinson et al., Two communication antennas for the Viking lander spacecraft, *1974 IEEE Antennas and Propagation Symposium Digest*, vol. 12, June 1974, pp. 214–216.

32. C. C. Kilgus, Multielement fractional turn helices, *IEEE Transactions on Antennas and Propagation*, vol. AP-16, no. 4, July 1968, pp. 499–500.

33. C. C. Kilgus, Resonant quadrifilar helix, *IEEE Transactions on Antennas and Propagation*, vol. AP-17, no. 3, May 1969, pp. 349–351.

34. A. A. Oliner, Equivalent circuits for discontinuities in balanced strip transmission line, *IRE Transactions on Microwave Theory and Techniques*, vol. MTT-3, March 1955, pp. 134–143.

35. J. S. Rao and B. N. Ras, Impedance of off-centered stripline fed series slot, *IEEE Transactions on Antennas and Propagation*, vol. AP-26, no. 6, November 1978, pp. 893, 894.

36. J. Van Bladel, Small hole in waveguide wall, *Proceedings of IEE*, vol. 118, January 1971, pp. 43–50.

37. P. K. Park and R. S. Elliott, Design of collinear longitudinal slot arrays fed by boxed stripline, *IEEE Transactions on Antennas and Propagation*, vol. AP-29, no. 1, January 1981, pp. 135–140.

38. H. E. King and J. L. Wong, A shallow ridged-cavity cross-slot antenna for the 240- to 400-MHz frequency range, *IEEE Transactions on Antennas and Propagation*, vol. AP-23, no. 5, September 1975, pp. 687–689.

39. C. A. Lindberg, A shallow-cavity UHF crossed-slot antenna, *IEEE Transactions on Antennas and Propagation*, vol. AP-17, no. 5, September 1969, pp. 558–563.

40. R. C. Hansen, ed., *Microwave Scanning Antennas*, Vol. II, Academic Press, New York, 1966.

41. R. F. Harrington, *Time-Harmonic Electromagnetic Fields*, McGraw-Hill, New York, 1961, p. 69.

42. A. F. Stevenson, Theory of slots in rectangular waveguides, *Journal of Applied Physics*, vol. 19, January 1948, pp. 24–38.

43. A. Dion, Nonresonant slotted arrays, *IRE Transactions on Antennas and Propagation*, vol. AP-7, October 1959, pp. 360–365.

44. R. C. Hansen, in A. W. Rudge et al., eds., *The Handbook of Antenna Design*, Vol. II, Peter Peregrinus, London, 1983.

45. M. J. Ehrlich, in H. Jasik, ed., *Antenna Engineering Handbook*, McGraw-Hill, New York, 1961.

46. R. S. Elliott and L. A. Kurtz, The design of small slot arrays, *IEEE Transactions on Antennas and Propagation*, vol. AP-26, no. 2, March 1978, pp. 214–219.

47. R. S. Elliott, On the design of traveling-wave-fed longitudinal shunt slot arrays, *IEEE Transactions on Antennas and Propagation*, vol. AP-27, no. 5, September 1979, pp. 717–720.

48. R. S. Elliott, An improved design procedure for small arrays of shunt slots, *IEEE Transactions on Antennas and Propagation*, vol. AP-31, no. 1, January 1983, pp. 48–53.